uc3m | Universidad Carlos III de Madrid

Escuela Politénica Superior

Degree in Aerospace Engineering

A numerical study on transverse gusts at low Reynolds number

Bachelor tesis

Author:

Manuel Florentin Olaru

Supervisor:

Manuel Moriche Guerrero

Leganés, September 2018

Abstract

The emerging design of MAVs has arisen a great interest in making research about unsteady Aerodynamics of flapping wings at low Re. When MAVs are flying in real conditions in the atmosphere, they have to face winds' unsteadiness such as continuous turbulence or discrete gusts.

The purpose of this thesis is to better understand the physics behind a gust encounter at low Reynolds number. For that, direct numerical simulations are carried out for different transverse gusts with large amplitudes, where the gust velocities are comparable to the freestream velocity. In addition, two different setups are prepared for DNSs and their results are compared with similar experiments from the literature. A third setup for DNS is presented conceptually as well.

For the DNS results, a parametric study is done in terms of gust intensity. After analyzing the aerodynamic forces during the gust encounters, some models are developed to predict the lift force during and after the gust encounter.

Contents

List of Figures

List of Tables

Glossary

2D Two Dimensional.

3D Three Dimensional.

CFD Computational Fluid Dynamics.

DLM Doublet Lattice Method.

DNS Direct Numerical Simulation.

GR Gust Ratio.

IBM Immersed Boundary Method.

LE Leading Edge.

LES Large Eddy Simulation.

LEV Leading Edge Vortex.

LHS Left Hand Side.

MAV Micro Air Vehicle.

RANS Reynolds Averaged Numerical Simulation.

RHS Right Hand Side.

TE Trailing Edge.

TEV Trailing Edge Vortex.

TUCAN Two/Three-Dimensional Unsteady Code for Aerodynamics in Nature.

Chapter 1

Introduction

1.1 Motivation

The recent development of Micro Air Vehicles (MAVs) has driven the scientific community to make research about the unsteady Aerodynamics of flapping wings in the last two decades, which is not properly understood to date. The term MAV stands for very small and remotely controlled, unmanned aircrafts. Their largest dimension shall not exceed 15 centimeters [19, 22].

The use of micro air vehicles has many purposes [21]: surveillance, security, reconnaissance and warfare, among many others. Their wide range of applications spans from civil to military missions. The continuous development of MAVs is driven by the desire for low-cost, feasible and low altitude aerial surveillance. However, MAVs sometimes experiment unpredictable flight behaviors, so there is a need for implementing a proper flight control system in order for MAVs to operate optimally in a wide range of missions and environments. A fundamental problem related with flight stability is the response of MAVs to gusts. Current knowledge about the interaction of these vehicles and winds' unsteadiness is very limited, so control models of MAVS usually do not take into account the aerodynamics governing a gust encounter.

Since MAVs fly at low velocities and the reference lengths are quite modest, the chord-based Reynolds number $Re = \frac{U_\infty c}{\nu}$ of the flow is relatively small compared to conventional airplanes. In particular, for rigid flapping-wings, Re ranges between 10^1 and 10^4 [22]. Thus, the aerodynamics of MAVs differ from the high Re aerodynamics of aircrafts and it is more complex, specially in the case of flapping-wings MAVs. For the case of small amplitude motions at high Re, where usually

no separation occurs, the flow is fully understood and there are a lot of models (Theodorsen, Wagner, Kussner...) for those type of flows. However, the problem appears for flows at low Re with high amplitudes of motion at moderate frequencies, which is the current problem of insects and birds flight. Then, the fundamental differences do not lie only on the Reynolds number of the flow, but also on the lift to drag ratio and sensitivity to high-amplitude gusts [24], where the transverse gust velocities are comparable to the free-stream velocity.

Many MAVs have fixed and rotary wings besides flapping configurations. It is convenient to use flapping-wing configurations because they are able to generate both thrust and lift at once [22] and they are more efficient than rotary configurations. Compared to fixed-wing configurations,there is not any need for these devices to have a propulsive system such as conventional aircrafts do, i.e. implement a pair of propellers or jet engines.

Understanding the insect and bird fly can help us designing flapping-wing MAVs, then the research about unsteady Aerodynamics at low Re is highly beneficial.

There are some challenges in terms of aerodynamics for MAVs flying in real conditions [24]. Gusts and wind unsteadiness over short durations are natural phenomena occurring near flying objects within the Earth's boundary layer. MAVs need to remain stable and maneuverable in those situations, which results in a very complicated problem. Concerning gust encounters, we can have longitudinal, transversal, periodic and discrete gusts. In order to simplify the problem, it was decided to focus on the interaction between discrete transverse gusts and wings as a previous step for designing a proper response of the vehicle.

In summary, taking into account the flying speeds of MAVs, flow disturbances such a gust may be of the same order as the free stream velocity. The unsteady aerodynamics of gust encounters of conventional aircrafts cannot be applied because assumes small disturbances of the flow and do not capture viscous phenomena, as previously pointed out above. Therefore, the physics behind the interaction of these low Reynolds number flyers and unsteady free streams is not properly understood, so a good starting point is studying the aerodynamic forces on airfoils during transverse gust encounters and try to predict them.

1.2 State of the art

Nowadays, the accuracy of existing models to predict the aerodynamic forces of large-amplitude motions at low Re is unsatisfactory. The same applies for gust response of MAVs.

Typical high-lift mechanisms involved in low Re unsteady aerodynamics are delayed stall, wake capture and clap and fling [8, 23]. Before proceeding with the state of the art, some features of flapping kinematics must be introduced. Flapping motion of an airfoil can be considered as the superposition of pitching and plunging motion. Concerning the heaving motion, a flapping cycle consists on a downstroke (first half of a period) and an upstroke (second half). The delayed stall or dynamic stall phenomena is of particular interest and relevance, in which a leading edge vortex (LEV) appears on the upper surface of the wing while it descends, or better said, when the effective angle of attack is higher than a specific threshold. This vortex creates a low pressure zone on the suction surface and it significantly enhances the aerodynamic forces throughout the downstroke followed by a sudden drop, which has been shown experimentally [6, 10] and computationally [16, 30]. The role here of the LEV is similar to the case of high Re flow around delta wings [3].

Concerning the LEV, the situation is more complex for three-dimensional cases. Following [10], there have been several follow-up investigations in order to analyze the role played by the LEV in 3D cases. Shyy et al. [25] analyzed the behavior of the LEV, comparing results with previous works and conclusions with three-dimensional direct numerical simulations (DNSs). They found out that LEVs are typical flow structures for flapping wings flying at Re of $O(10^4)$ or lower. For Re of $O(10^3$ *to* $10^4)$, the LEV breaks down approximately at a spanwise location of three quarters of the span towards the wing tip, as [5, 27, 29] agree as well. The LEV needs to maintain a high axial flow velocity in the core and remain stable in order to be effective for lift augmentation while plunging. On the other hand, for Re of $O(10^2)$, the LEV is not that prone to detach and it is connected to the wing tip vortex, as stated by [5]. The detachment of the LEV and its break down is related to a weak spanwise axial flow and to smaller spanwise pressure gradient.

Regarding the interaction between wings and gusts, many studies do not take into account the stiffness of the wing and assume the wing is rigid rather than elastic (deformable), reducing the real aeroelastic problem to an isolated aerodynamic problem. The next strong assumption is the reduction of the three-dimensional character of the wing to a two-dimensional problem, only valid for an airfoil or a wing of infinite aspect ratio, assuming the flow to be strictly 2D. Note that all these simplifications are done in order to tackle the real and complex problem. In spite of these strong assumptions, the parametric space is still huge: airfoil angle of attack (AoA), gust field, Re, etc.

Nevertheless, the assumption of two-dimensional flow might be correct at low Re. For instance, for the case of the flow past a circular cylinder of infinite span, three-dimensional effects appear at Re of 200 approximately [32]. Hoarau et al.[12]

studied the incompressible flow over a NACA0012 infinite aspect ratio wing at a 20 degrees angle of attack and discovered that 3D effects appeared at Re=800.

Concerning the computation of external flows over a certain aerodynamic body, one has the choice to recur to panel methods and to other computational techniques. Even with the evolution of computers, unsteady panel methods such as the Doublet Lattice Method (DLM) [2] cannot be used for flapping-wings aerodynamics or low Re number aerodynamics in general because they do not capture flow separation. Concerning conventional fixed-wing aircrafts, this successful method in its simplest version (no thickness modelling, boundary layer not modelled) is a key tool for computing unsteady flows even in the case of big manufacturers and designers such as the Airbus Group, in particular for the A400M. DLM is very powerful although it neglects thickness and viscosity effects, but those contributions cancel each other and let the method be very accurate when predicting aerodynamic forces over big airplanes flying at high speeds. However, back to the low-Re problem, this method is unsatisfactory because it would not be able to capture relevant features such as the LEV (boundary layer detachment) and, consequently, it will be a deficient way for computing aerodynamic forces.

Computational aerodynamics is a critical discipline within Aeronautics. Following the evolution of computer architecture and algorithms, the capability of solving flows numerically has improved extraordinarily during the last decades. Results from computational flow analysis complements experiments. The design of any aerial vehicle demands high precision and rapidity. Hence, the computational fluid dynamics (CFD) is an important part of the design. Within the field of computational aerodynamics, there are several approaches for the numerical computation of flows such as Reynolds Averaged Navier-Stokes (RANS), Large eddy simulations (LES) and Direct Numerical Simulations (DNS), among many others and variants [9]. One should be aware of the level of modelling of CFD techniques: RANS is the option with the highest amount of turbulence modelling, while the DNS procedure has zero modelling and the LES lies in between RANS and DNS in terms of the amount of turbulence modelling. Depending on the desired solution, simulations rely on one method or another. For instance, RANS works well for steady-state solutions for attached flows about complex geometry configurations or for unsteady cases where the flow is primarily attached around simpler geometries. Massive separations and vortex-dominated fluid domains are difficult to solve accurately using RANS. Solutions for separated flows are more accurate by using LES or variants such as hybrid RANS-LES. The use of LES and hybrid methods is increasing while DNSs are used on finer meshes.

The main disadvantage of DNS is the high computational cost. For instance, for a MAV, it is not viable the implementation of a DNS solver within the flight control

system in order to compute and predict aerodynamic forces due to limitations of mass, available space and time scales. Thus, MAVs need accurate models covering an entire flight envelope so that the device can operate optimally in different scenarios.

The first attempts to study gusts on airfoils were conducted at the end of the 1930's: the birth of unsteady thin airfoil theory. Küssner [15] estimated the increase of lift on a thin airfoil while entering a sharped edge gust. Von Karman and Sears [14] theoretically computed the lift on a thin airfoil due to a sinusoidal gust. However, the unsteady thin airfoil theory is not capable of predicting viscous phenomena such as the LEV effect, or boundary layer sepparation in general, due to its strong assumptions: inviscid flow, small displacements/perturbations. Especially in 3D cases with deep stall, there is a poor agreement between the unsteady thin airfoil theory and real results from flapping flight at low Re [33].

With the development of MAVs and the emerging awareness of gust sensitivity of these devices [24], there are recent works which try to quantify and model the forces around wings exposed to large transverse gusts of the order of the free stream velocity at Re of $O(10^4)$. Perrotta and Jones [20] studied the effects of intense transverse gusts on a flat-plate of AR=4 experimentally at the University of Maryland's hydrodynamic tunnel using particle imaging velocimetry (PIV). They modeled the transverse gust as the canonical discrete "sine squared" profile used in aircraft industry [13]. Once the shape of the gust velocity has been chosen, there are two remaining parameters to set for a particular gust: the gust width or length w, which can be expressed in terms of chord lengths, and the gust ratio GR. The gust width is commonly referred in the aeroelasticity's literature as twice the 'gust gradient' H [13]. The gust ratio GR is the ratio between the peak velocity value of the discrete gust and the freestream velocity. The test cases analyzed by Perrotta and Jones [20] were conducted at $Re = \frac{U_\infty c}{\nu} = 10,000,\ 20,000$ and $40,000$, with associated $GR = 1.68,\ 0.84$ and 0.42, respectively, with several angles of attack. All their experiments were conducted with a gust ratio $w/c = 3.18$. Their tests show the emerging of the LEV while the wing entered the gust, with the expected lift peak and sudden drop afterwards. The ultimate goal of [20] was the development of force prediction models, choosing the most relevant parameters the magnitude of the peak force produced by the LEV and the time recovery of the flow after the wing exits the gust, focusing more on the lift rather than the drag. Concerning both aerodynamic forces, the peak values were properly predicted by a quasi-steady and empirical model based on lift and drag static data. However, this quasi-steady model was not able to capture the gust recovery process after the wing exits the gust. Regarding the recovery process after the gust, an empirical version of the convolution with Kussner's function in the time domain under-

predicted the duration of transient effects after the gust.

Following the experiments of Perrotta and Jones [20], Biler et al. [4] performed similar experiments at the same site (University of Maryland's hydrodynamic tunnel) with the same flat-plate, together with computational simulations done with an in-house and open source Navier-Stokes solver OVERTURNS developed at the University of Maryland. Both experiments and simulations were performed at $Re = 40,000$ with a different gust width this time, $w/c = 4$. The test cases combined different gust ratios up to $GR = 0.37$ and wing angles of attack $AoA = [0^o, 45^o]$. Their Navier-Stokes solver was validated with previous studies and the results from the experiments and computations agree well with each other, so the results in [4] can be taken as a benchmark. The goal of these experiments was not the elaboration of predictive models as in the case of Perrotta and Jones [20], but it was a deeper understand of the physics behind gust encounters at low Re. Note that this time the gust ratios were not very intense ($GR_{max} = 0.37$) as in the previous study ($GR_{max} = 1.68$) [20]. Biler et al. [4] found that increasing the gust ratio, the peak value of the lift increases as well, but only for geometric wing AoA up to 20^o. As pointed out in [20], Biler et al. confirmed the fact that peak values of lift and drag depend on leading edge effective angle of attack rather that gust ratio or wing geometric AoA.

The previous two studies did not used the air as working medium but water. The reason why water was used is because the forces are higher and the aerodynamic coefficient are more accurate. There are facilities where air is the working medium for these kind of experiments, as the wind-tunnel from the US Army Research Laboratory [26] or the one at the University of Florida [11]. Both are intended to study unsteady aerodynamic phenomena at low Re for MAV research.

1.3 Objectives

The ultimate goal of this project is to increase our knowledge about transverse gust encounters at low Re, studying the forces during and after a gust encounter and try to predict them with simple models. For that, we will study the aerodynamic forces on a NACA0012 airfoil while it enters and exits a discrete sine-squared shape gust. The remaining parameters governing the problem are:

- Reynolds number
- Gust ratio $GR = \frac{peak\ gust\ velocity}{free-stream\ velocity}$
- Gust width w

- Airfoil geometric angle of attack α_0

For all the main test cases, we will use $Re = 1000$, $w/c = 3.2$ and $\alpha_0 = 5^o$. Therefore, the parametric study will focus on the effects of gust ratio.

After analyzing the forces and the vortex dynamics, the next step is to elaborate predictive models for the aerodynamic forces.

Apart from the primary objectives, there are secondary objectives such as:

- Understand what a numerical method is.
- How a DNS solver such as TUCAN works.
- Learn the differences between high-speed aerodynamics of conventional aircrafts and low Re aerodynamics.
- Understand that a model cannot reflect the reality; be aware of the advantages and disadvantages of each model.

1.4 Structure of the document

This thesis is organized as follows:

- Chapter 2 describes part of the methodology used in this work, from the governing equations and flow solver to the problem definition and predictive models. It summarizes the basics of the flow solver and it explains how it is used in order to obtain the results in chapter 3. After that, it presents two simple models for predicting the lift force during and after a gust encounter.
- Chapter 3 illustrates the results for all the cases from the first DNS setup. It undergoes a deep analysis for a reference case and makes a parametric study of the data sample.
- Chapter 4 presents the methodology for a second setup for gust modelling with TUCAN and it also presents conceptually a third approach. After that, the results are analyzed and compared with the previous ones. Finally, a comparison with results from literature is carried out as well.
- Chapter 5 shows the performance of the predicting models, analyzing their strong and poor aspects.
- Chapter 6 makes an analysis for the regulatory framework related to this work and illustrates the socio-economic impact of the thesis.

- Finally, chapter 7 makes a summary of the project and it presents some final conclusions.

Chapter 2

Methodology

2.1 Governing equations

The flow around an airfoil for MAV design can be considered to be incompressible [31], so the equations governing the fluid motion are the incompressible Navier-Stokes equations:

$$\frac{\partial u_i}{\partial x_i} = 0 \tag{2.1}$$

$$\frac{\partial u_i}{\partial t} + u_j \frac{\partial u_i}{\partial x_j} = -\frac{1}{\rho}\frac{\partial p}{\partial x_i} + \nu \frac{\partial^2 u_i}{\partial x_i^2} \tag{2.2}$$

where x_i is the cartesian coordinate, u_i is the velocity component, p is the pressure, ρ is the fluid density and ν is the kinematic viscosity of the fluid.

2.2 Numerical method and flow solver

The flow is solved by means of a two dimensional Direct Numerical Simulation (DNS). Since the Reynolds number of the flow based on the free-stream velocity and the chord length is 1000, a DNS is feasible. Although we get very accurate results with DNS, the computational cost is significant. It was decided not to use a turbulence model because we can carry the simulations of this project with a DNS.

For the purpose of this work, the solver to be used is TUCAN: an in-house unsteady, viscous and incompressible tool to perform DNS, developed by M. Moriche, PhD [18]. TUCAN is validated with the 2D Poiseuille flow, among others. TUCAN, or any proper DNS solver, is capable to capture key features of the unsteady flow at low Re such as leading edge and trailing edge vortices [18]. In addition, the version of TUCAN used for this work adopts the implementation provided by A. Gonzalo for using a non-uniform grid for spatial discretization.

The spatial discretization is done with second order, centered finite differences with a non-uniform, staggered and structured grid. Temporal discretization is performed with a three-stage and low-storage Runge-Kutta scheme, in which the diffusion terms from the momentum equation are treated implicitly and the advective ones are treated explicitly. Then, the scheme is referred as semi-implicit.

In order to fulfill the continuity equation, which is not time dependent, Brown et al. [7] proposed a fractional step method consisting of obtaining the velocity from the momentum equation, and then apply a correction to accomplish both continuity and momentum equations.

2.2.1 Modelling of submerged bodies

The first part of this chapter dealt with the Navier-Stokes equations without considering the presence of bodies within the fluid domain. TUCAN uses an immersed boundary method (IBM) with direct forcing proposed by M. Uhlmann [28] rather than using body-fitted grids. The incompressible N-S equations are obviously the same, but we introduce a volumetric force term in the RHS of the momentum equation. This implementation in the software makes the analysis more efficient at low Re regimes and the difficulty of grid definition of complex and moving geometries is totally removed since we do not use body-fitted grids. This algorithm must be introduced in the Runge-Kutta scheme for complete flow solving. The motion of the submerged bodies is easily implemented by the user.

The peculiarity of this flow algorithm is that it does not impose the non-slip boundary condition on the airfoil directly, it enforces this condition by the use of a forcing term on the RHS of the momentum equation. TUCAN uses two independent meshes: an Eulerian and a Lagrangian mesh. The Eulerian mesh is the fluid mesh itself, and the Lagrangian mesh is the "body" mesh which consists of forcing points along the airfoil surface. The flow is solved in the Eulerian mesh by making interpolations with the Lagrangian mesh via regularized delta function.

The steps of the algorithm for the IBM can be summarized as follows:

1. Make an explicit estimation of the flow velocity in the Eulerian mesh.
2. Interpolate the estimated velocity to the Lagrangian frame to evaluate the estimated velocity at the Lagrangian points.
3. Compute the forcing term in the Lagrangian frame required to obtain the desired velocity to fulfill the non-slip boundary condition at each Lagrangian marker.
4. Spread the forcing term from the Lagrangian to the Eulerian frame
5. Solve the Navier-Stokes equations in the Eulerian frame including the volumetric force term within the RHS of the momentum equation.

2.3 Problem definition

It was decided to perform a 2D DNS of the flow around a symmetric airfoil NACA 0012. The Reynolds number of the flow is $Re = cU_\infty/\nu = 1000$, where c is the airfoil chord, U_∞ is the free stream velocity and ν is the kinematic viscosity of the fluid. All the simulations are carried out with TUCAN.

The simulations try to model a discrete tuned gust with "1-cosine" shape, which is the typical design gust profile for flying vehicles [1]. The gust encounter is depicted in figure 2.1. Concerning the reference frame used, the observer does not move with the airfoil.

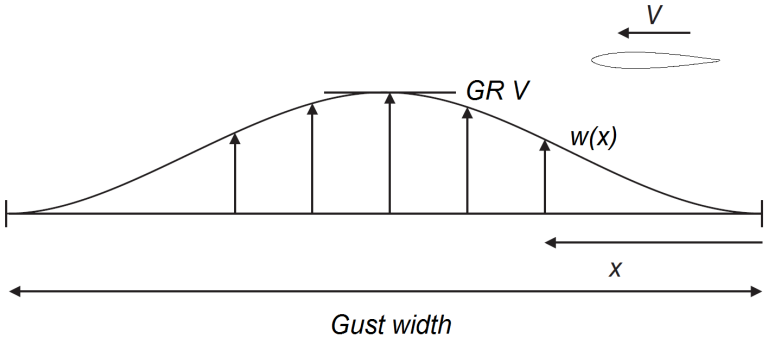

Figure 2.1: Shape of a '1-cosine' discrete gust

The vertical velocity profile of the gust in terms of the spatial coordinate x is given by

$$w_g(x) = \begin{cases} \frac{GR\ U_\infty}{2}\left(1 - cos\left(\frac{2\pi x}{w}\right)\right) & \text{if } x_0 < x < x_0 + w \\ 0 & \text{otherwise} \end{cases} \tag{2.3}$$

where x_0 is the location of the beginning of the gust, GR is the gust ratio and w is the longitudinal gust width. The gust ratio represents the ratio between the maximum gust velocity $w_{g,max}$ and the free stream velocity U_∞.

The corresponding temporal variation of gust velocity seen by the airfoil, taking into account that $x = U_\infty t$, is

$$w_g(t) = \begin{cases} \frac{GR\ U_\infty}{2}\left(1 - cos\left(\frac{2\pi U_\infty t}{w}\right)\right) & \text{if } t_0 < t < t_0 + w/U_\infty \\ 0 & \text{otherwise} \end{cases} \tag{2.4}$$

where t_0 is the time instant at which the gust appears.

As the airfoil enters the gust, the local effective angle of attack $\alpha_{eff}(x)$ along the chord line changes due to the induced angle of attack α_i produced by the gust velocity:

$$\alpha_{eff}(x) = \alpha_0 + \alpha_i = \alpha_0 + arctan\left(\frac{w_g(x)}{U_\infty}\right) \tag{2.5}$$

where α_0 is the geometric angle of attack of the airfoil.

This setup is very complicated, so we introduce another method based on plunge maneuvers for gust modelling which simplifies the setup and does not require a very high computational cost. Chapter 4 introduces improved, more realistic approaches for modeling the setup described above. Thus, this chapter will present the methodology for gust modeling only via heave maneuvers.

This first modeling approach for '1-cosine' discrete transverse gust moves the airfoil downwards with the same vertical velocity as the one prescribed by the gust profile. This heaving motion can be implemented in TUCAN by prescribing the vertical motion of the Lagrangian points located along the airfoil's surface. Therefore, we need to integrate the gust profile velocity in order to get the vertical position of the airfoil during the plunge maneuver. After integration of equation (2.4) and changing its sign (the gust velocity goes upwards, but the heaving motion goes downwards), we obtain the motion of the airfoil:

$$z(t) = \begin{cases} 0 & t < t_0 \\ \frac{GR\ w}{4\pi} sin\left(\frac{2\pi U_\infty t}{w}\right) - \frac{GRU_\infty t}{2} & t_0 < t < t_0 + w/U_\infty \\ -\frac{GRw}{2} & t > t_0 + w/U_\infty \end{cases} \tag{2.6}$$

Since TUCAN works with non-dimensional equations, eq.(2.6) must be dimensionless:

$$\tilde{z} = \frac{z}{c} = \begin{cases} 0 & \tilde{t} < \tilde{t}_0 \\ \frac{GR}{4\pi}\frac{w}{c} sin\left(\frac{2\pi\tilde{t}}{w/c}\right) - \frac{GR}{2}\tilde{t} & \tilde{t}_0 < \tilde{t} < \tilde{t}_0 + w/c \\ -\frac{GR}{2}\frac{w}{c} & \tilde{t} > \tilde{t}_0 + w/c \end{cases} \tag{2.7}$$

The non-dimensional set of parameters which define the problem is large: Re, GR, w/c, α_0. To make the problem easier, we only vary the gust ratio from $GR = 0.05$ to $GR = 1.68$. For that, the Reynolds number is $Re = 1000$, the gust width is $w/c = 3.2$, the geometric AoA is $\alpha_0 = 5^o$. The cases for this type of simulations are depicted in tables 3.1 and 3.2.

2.4 Computational setup

Concerning the plunge maneuvers, the simulations are performed in a domain of dimensions $[12c \times 9.5c]$ in the streamwise and vertical directions, respectively. The domain in the x direction (streamwise) goes from $x/c = -3.5$ to $x/c = 8.5$ and in the z direction goes from $z/c = -6.5$ to $z/c = 3$. Before the heaving motion, the airfoil's LE is placed at $x/c = 0$ and $z/c = 0$. After the plunge maneuver, the airfoil's new vertical position is dictated by equation (2.7). The lowest vertical position of the airfoil during the plunge maneuvers is at $z/c = -2.69$. Note that the reference point for the vertical position of the airfoil, which will be used throughout this document, is the leading edge. The fluid domain is depicted in figure 2.2.

The Eulerian mesh contains a total of 750×882 grid points in the x and z directions, respectively. As mentioned in section 2.2, the spatial discretization is done on a cartesian, structured, non-uniform, staggered grid. The resolution is not uniform: $d\tilde{x} = dx/c$ varies streamwise, and the same occurs with $d\tilde{z} = dz/c$ vertically. From $x/c = -0.5$ to $x/c = 2$, the resolution is uniform, with 160 points per chord length ($d\tilde{x} = 1/160$). As we go upstream $x/c = -0.5$ or downstream $x/c = 2$, $d\tilde{x}$ increases linearly (a stretching factor is applied) so that $d\tilde{x} = 1/19.425$ for $x/c \in [-3.5; -2.1]$ and $d\tilde{x} = 1/19.8$ for $x/c \in [6.4; 8.5]$. In other words, the mesh is very fine around the airfoil and relatively coarser far away in the streamwise direction. Note that the upstream and downstream stretching factors are not the same: downstream the airfoil we need a lighter stretching because vortices will travel through that zone of the domain. In a similar way is done with $d\tilde{z}$: the finest zone is located between $z/c = -2.8$ and $z/c = 0.5$ with constant $d\tilde{z} = 1/160$. A stretching factor is applied vertically for $z/c > 0.5$ and $z/c < -2.8$ so that the mesh is

coarser. Concerning the resolution of 160 grid points per chord length within the refined zones, recent researches of unsteady aerodynamics at Re=1000 [18] used a resolution of 128 grid points per chord length, so using 160 instead of 128 does not affect negatively the accuracy of the results presented in this thesis.

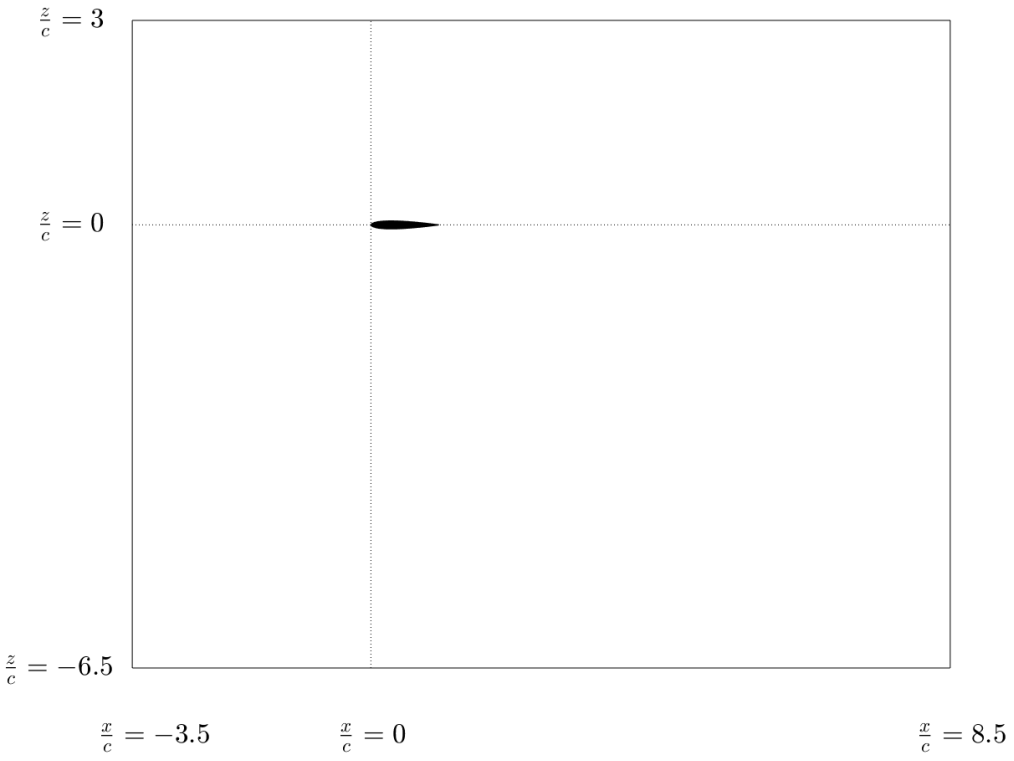

Figure 2.2: Computational domain of the plunge maneuvers

Regarding the boundary conditions shown in figure 2.3, a uniform free stream velocity $u = U_\infty, w = 0$ is imposed at the inlet boundary, located $3.5c$ upstream the airfoil. The outflow, at $x/c = 8.5$, is modelled with an advective boundary condition. With this last condition, we minimize the reflections that may affect the solution of the problem, which would be the case of either Dirichlet or Neumann boundary conditions at the outlet [18]. Concerning the north and south boundaries of the domain, a free slip condition is imposed at those boundaries ($\partial u/\partial z = 0, w = 0$). The initial conditions are $u = U_\infty, w = 0$ everywhere.

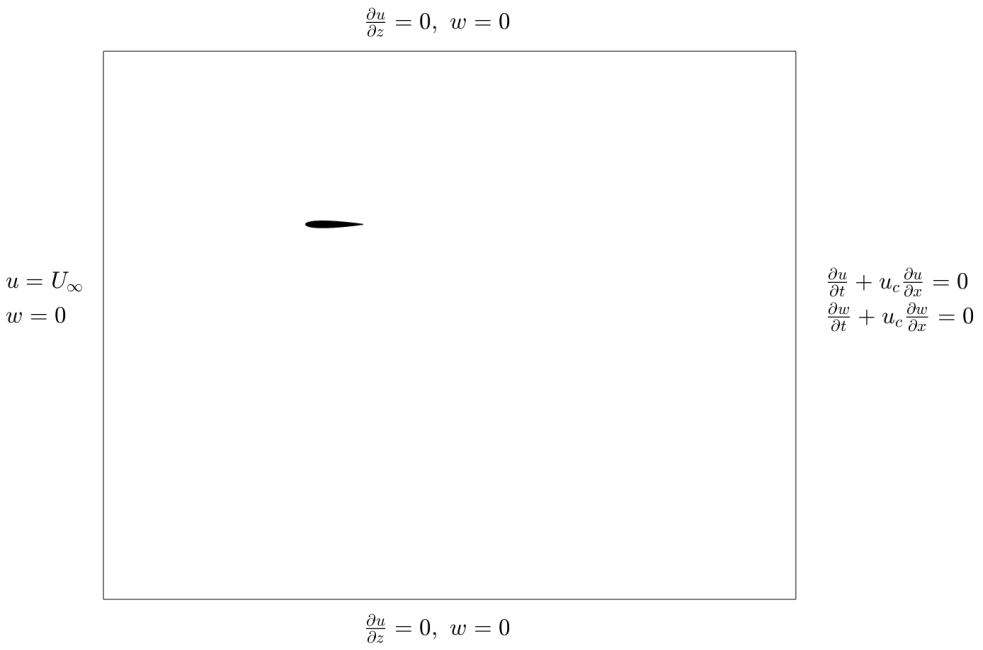

Figure 2.3: Boundary conditions for the first computational setup

The NACA0012 airfoil is discretized by a uniform distribution of points, i.e. equispaced Lagrangian force points along its surface. Each forcing point has to control a volume ΔV_l in the Lagrangian frame equivalent to a volume within the Eulerian mesh. As recommended by M. Uhlmann [28] for the case of a circumference, ΔV_l must be as close as possible to ds^2. Keeping in mind the desired resolution $dx/c = 1/160 = 6.25 \cdot 10^{-3}$, we distribute 326 points along the entire airfoil surface with $ds/c = 6.256 \cdot 10^{-3}$. The associated volume to each Lagrangian marker is $\Delta V_l/c^2 = 3.9102 \cdot 10^{-5}$, which is very close to $(ds/c)^2 = 3.9141 \cdot 10^{-5}$ (an error of -1%).

2.5 CFL analysis

There is an important parameter of the simulations which is very bound to the time step $d\tilde{t} = U_\infty dt/c$: the Courant Fredrich Levy number (CFL). The CFL of each cell within the grid is defined as

$$CFL = \frac{max(|u_x|, |u_y|, |u_z|)\Delta t}{\Delta x} \tag{2.8}$$

This parameter is computed at each time step and at each cell. The CFL of each time step is the global maximum CFL among all the local CFLs computed throughout the fluid domain. Regarding the meaning of this number, it describes how fast a fluid particle moves in a time step. For instance, if $CFL = 1$, then one particle travels a distance equal to dx in one time step dt. This is undesirable, so the CFL must be lower than 1 for stability reasons, so that the DNS outputs reliable results. In particular, we want the simulations to have $CFL < 0.5$ all the time. The CFL of the flow prior to the heaving maneuver, CFL_0, will be a parameter to distinguish different cases. On top of the constraint of small CFL, the IBM shows some sensitivity to the CFL that will be studied in the next chapter.

A third approach is thought to implement in TUCAN for gust modelling, which is described in the Chapter 4.

2.6 Description of predictive models for gust encounters

Direct numerical simulations require a considerable computational cost and time for solving the N-S equations accurately. Using reduced-order models may help us to get similar results with a very low computational cost, and a lot faster. However, the drawback of these models is that they may work very well for certain Re range or very specific gusts, i.e. a model made for a particular gust at a certain Re number may deteriorate if we change the Re number or the gust profile. Predictive models are a key component for designing a flight control systems for a MAV covering a large gust envelope. As mentioned in the Introduction, current MAV's size, weight and dimensions make it impossible for having a N-S solver within the electronic control block of the vehicle.

Chapter 5 presents different approaches to predict the lift history during a gust encounter, knowing the velocity profile of the gust. The analysis focuses on the increment of lift Δc_l, which is the force always perpendicular to the far-field free stream velocity U_∞.

In this project we elaborate two simple models: a semi-empirical quasi-steady one and an unsteady one using a convolution approach with Kussner and Wagner functions.

For both models, apart from the shape of the gust, we need as input a database of lift values for different effective angles of attack. It is chosen to use three different inputs as lift data: thin-airfoil theory, data from experiments of Perrotta

and Jones [20] and data from XFLR5 for a NACA0012 airfoil. As mentioned in the previous chapter, although the data published in [20] applies for a flat plate of aspect ratio 4, a transformation can be applied to convert wing aerodynamic coefficients to airfoil-equivalent values.

2.6.1 Quasi-steady model

The lift c_l and drag c_d coefficients treated in this work are always oriented and non-dimensionalized according to the free-stream velocity U_∞, not the total velocity seen by the airfoil during the gust. The three data inputs (thin-airfoil theory, data from [20] and XFLR5) provide lift and drag curves where the lift $\tilde{c}_l$ and drag $\tilde{c}_d$ coefficients belong to a force which is always perpendicular or parallel to the total incoming flow (classical convention for aircraft's aerodynamics) and which is non-dimensionalized by the square of the modulus of the total incoming flow.

The steps taken in this model are the following:

- First get the evolution of the leading edge effective angle of attack during the gust.
- Use one of the lift databases to construct $\tilde{c}_l(\tilde{t})$ and $\tilde{c}_d(\tilde{t})$.
- Once it is known the history of $\tilde{c}_l(\tilde{t})$, we must re-orient the force so that it is always perpendicular to the free-stream velocity U_∞.
- The last step is changing the velocity non-dimensionalization.

The expression for the lift coefficient of the quasi-steady model is:

$$c_{l_{qs}}\left(\tilde{t}\right) = \left[\tilde{c}_l\left(\tilde{t}\right) cos(\alpha_i) + \tilde{c}_d\left(\tilde{t}\right) sin(\alpha_i)\right]\left[1 + \left(\frac{w_g}{U_\infty}\right)^2\right] \tag{2.9}$$

Then, the increment of lift exported by the model will be

$$\Delta c_{l_{qs}}\left(\tilde{t}\right) = c_{l_{qs}}\left(\tilde{t}\right) - c_{l_{qs}}\left(\tilde{t}=0\right) \tag{2.10}$$

2.6.2 Unsteady, indicial model

The second model uses a convolution integral which is frequently used in the field of unsteady thin airfoil aerodynamics and aeroelasticity [1, 13]

$$\Delta c_{l_{us}}\left(\tilde{t}\right) = \int_0^{\sigma=\tilde{t}} \frac{dc_{l_{qs}}}{d\sigma} \psi\left(2\left(\tilde{t}-\sigma\right)\right) d\sigma \tag{2.11}$$

where σ is a dummy variable for the convective time $\tilde{t}$ and ψ may be the Kussner or Wagner function. For the plunging maneuvers, it makes sense to use Wagner function as the airfoil sees the same effective angle of attack along the chord line. Concerning the jet gust case, Kussner function is a better candidate since the effective angle of attack is not the same along the chord line.

Chapter 3

Aerodynamic forces on airfoils during transverse gust encounters

This chapter presents the results from the cases simulated as plunge maneuvers. As explained in Chapter 2, this method is considered as the most suitable starting point for studying gust encounters from the point of view of the computational costs. Twenty-five cases were evaluated, making a sweep of gust ratios from $GR = 0.05$ to $GR = 1.68$. The purpose for having a plenty of gusts of different intensities is strictly related to the examination of the accuracy of predicting models for different gust ratios, as it will be seen further in Chapter 5. The first sixteen cases were simulations with different gust ratios, all of them with $CFL_0 = 0.08$. Meanwhile, it was observed that TUCAN is very sensitive to the time step, and consequently to the CFL of the flow. Therefore, it was decided to evaluate the influence of changes in CFL for two gust ratios: 0.42 and 1.68. As a result, an additional set of cases was added to the initial sixteen (see table 3.2). The first set of sixteen cases is detailed in table 3.1. The nomenclature for the cases hAGXXXwYYY_ZZZ follows these rules: "h" stands for heaving, "A" stands for geometric AoA=5º, "GXXX" denotes gust ratio of X.XX, "wXXX" means gust width w/c=X.XX and "_XXX" means CFL_0=X.XX. Recall that CFL_0 is an input; it represents the CFL value of the flow prior to the gust encounter and it is directly dependent on the time step $d\tilde{t}$ imposed by the user.

In order to compute aerodynamic coefficients, TUCAN yields streamwise and vertical forces which the fluid exerts on the airfoil at every forcing point, i.e. the Lagrangian markers along the airfoil's surface. The value of those forces are already non-dimensionalized with $\rho U_\infty^2 c$. Therefore, we defined the lift and drag coefficients as

$$c_l = \frac{-2\sum F_{z,\ forcing\ points}}{\rho U_\infty^2 c},\ c_d = \frac{-2\sum F_{x,\ forcing\ points}}{\rho U_\infty^2 c} \tag{3.1}$$

Note that lift and drag are considered to be always oriented parallel and orthogonal to the freestream velocity, respectively, even during the gusts, where the airfoil's incoming flow is not parallel to the free stream velocity.

Case	**Re**	α_0	**w/c**	**GR**	$\mathbf{CFL_0}$
hAG005w320_008	1000	5º	3.20	0.05	0.08
hAG010w320_008	1000	5º	3.20	0.10	0.08
hAG015w320_008	1000	5º	3.20	0.15	0.08
hAG021w320_008	1000	5º	3.20	0.21	0.08
hAG032w320_008	1000	5º	3.20	0.32	0.08
hAG042w320_008	1000	5º	3.20	0.42	0.08
hAG053w320_008	1000	5º	3.20	0.53	0.08
hAG063w320_008	1000	5º	3.20	0.63	0.08
hAG073w320_008	1000	5º	3.20	0.73	0.08
hAG084w320_008	1000	5º	3.20	0.84	0.08
hAG094w320_008	1000	5º	3.20	0.94	0.08
hAG105w320_008	1000	5º	3.20	1.05	0.08
hAG115w320_008	1000	5º	3.20	1.15	0.08
hAG126w320_008	1000	5º	3.20	1.26	0.08
hAG147w320_008	1000	5º	3.20	1.47	0.08
hAG168w320_008	1000	5º	3.20	1.68	0.08

Table 3.1: Sweep of gust ratios for plunge maneuvers

Signals exported by TUCAN have a considerable amount of noise due to the displacement of the forcing points. In order to suppress noise from the results, a correction is applied during post-processing of the results by means of a low pass filter ('loess' in MATLAB). This process is done in order to present "cleaner" results, i.e. the noise does not affect them, it is an artefact of the IBM. Figure 3.1 illustrates the difference between original data and smoother results. Hereinafter, the rectangular gray area of all the plots represents the time window at which the airfoil's LE is within the gust.

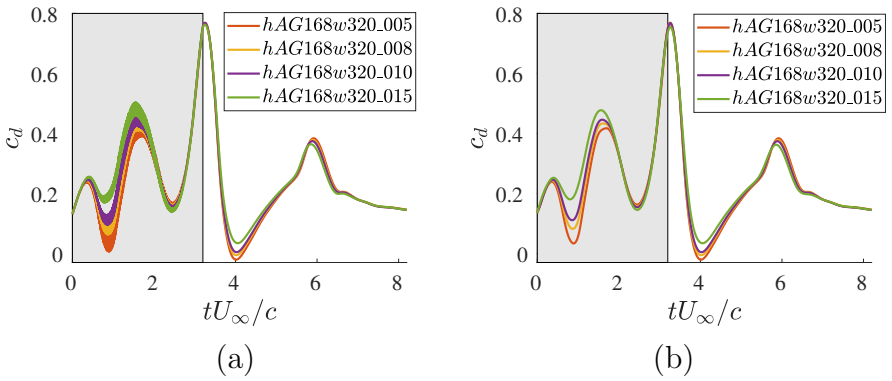

Figure 3.1: Comparison between results with noise (a) and after noise suppression (b)

The motion of the airfoil prescribed by equation (2.7) is depicted in figure 3.2. As we can see, the lowest position of the airfoil within the fluid domain is located approximately at $z/c = -2.6$ and the south boundary of the domain is located at $z/c = -6.5$, so the domain can be considered sufficiently large.

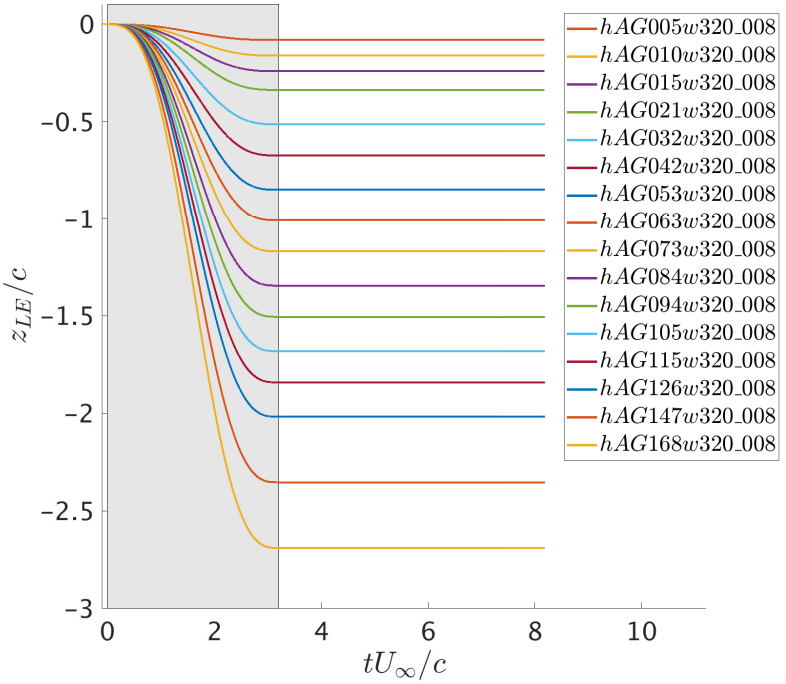

Figure 3.2: Vertical position of the airfoil during the plunge maneuvers

3.1 CFL analysis

This section proves the slight sensitivity of the TUCAN code to CFL. Table 3.2 collects all the cases used for the CFL analysis done for plunge maneuvers.

Case	Re	α_0	w/c	GR	CFL_0
hAG042w320_005	1000	5º	3.20	0.42	0.05
hAG042w320_008	1000	5º	3.20	0.42	0.08
hAG042w320_010	1000	5º	3.20	0.42	0.10
hAG042w320_015	1000	5º	3.20	0.42	0.15
hAG042w320_020	1000	5º	3.20	0.42	0.20
hAG042w320_025	1000	5º	3.20	0.42	0.25
hAG042w320_030	1000	5º	3.20	0.42	0.30
hAG168w320_005	1000	5º	3.20	1.68	0.05
hAG168w320_008	1000	5º	3.20	1.68	0.08
hAG168w320_010	1000	5º	3.20	1.68	0.10
hAG168w320_015	1000	5º	3.20	1.68	0.15

Table 3.2: Plunge maneuvers for CFL sensitivity

The sensitivity of the results to the time step is depicted in the figures below. As we can see, the TUCAN solver shows to be sensitive to changes in the time step dt. Even though the variations of c_d seem to be more significant (see figures 3.5 (a) and 3.5 (b)), they are nearly of the same order of magnitude as the lift variations. Although the differences in c_d values look like they are an issue, the absolute value of those differences are small compared to the net force values. With this, we are definitely aware of TUCAN's light sensitivity to the time step. Note that the variations in c_d occur in a time interval where c_l variations are negligible, and vice-versa.

As discussed earlier, the CFL is an accuracy-indicator of the DNS, along with the grid spatial discretization. Details about the CFL of the plunge maneuvers are shown in Fig. 3.6. It can be seen that all the cases are performed with a time step small enough in order to obtain accurate results. The worst scenario in terms of CFL is for $GR = 1.68$, but the highest CFL value for that case is lower than 0.25.

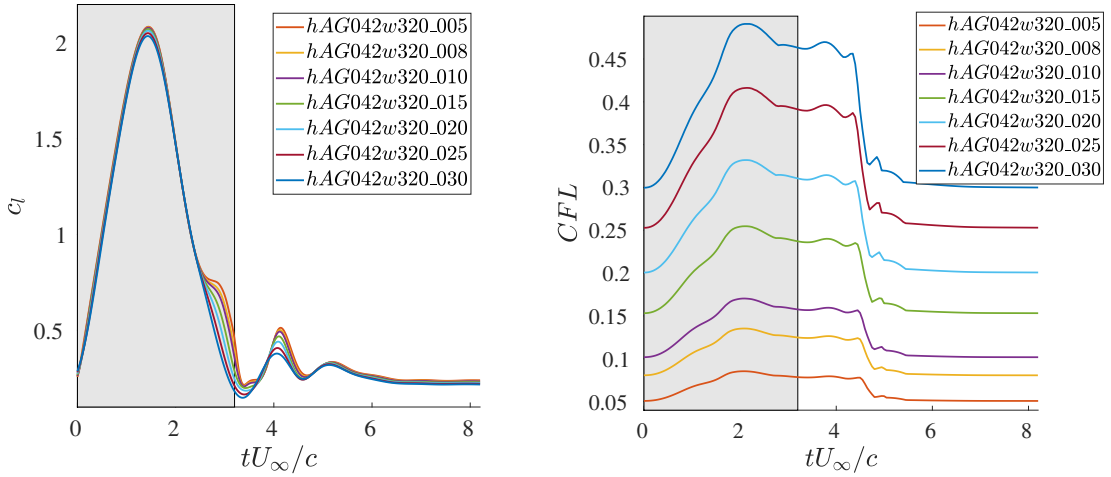

Figure 3.3: Sensitivity to time step: (a) c_l and (b) CFL for $GR = 0.42$

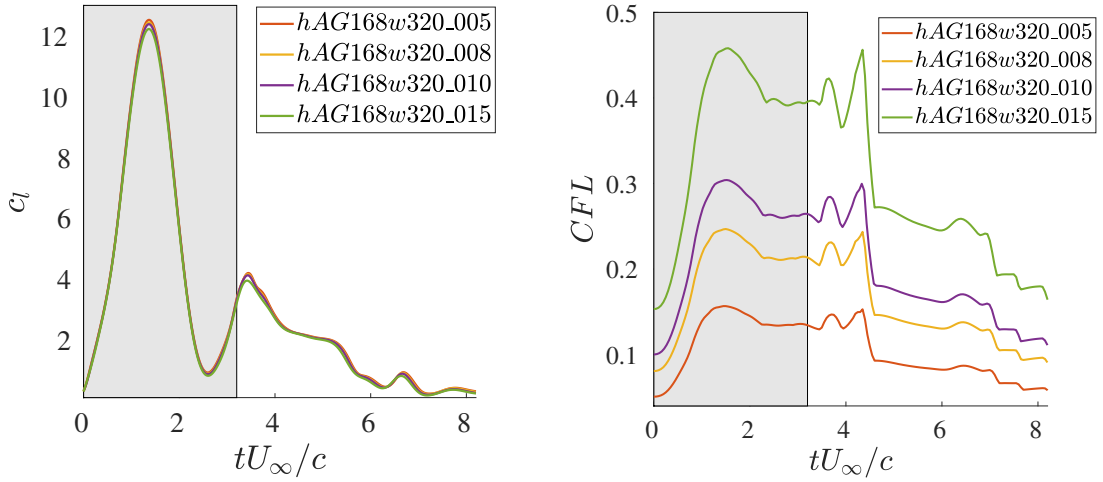

Figure 3.4: Sensitivity to time step: (a) c_l and (b) CFL for $GR = 1.68$

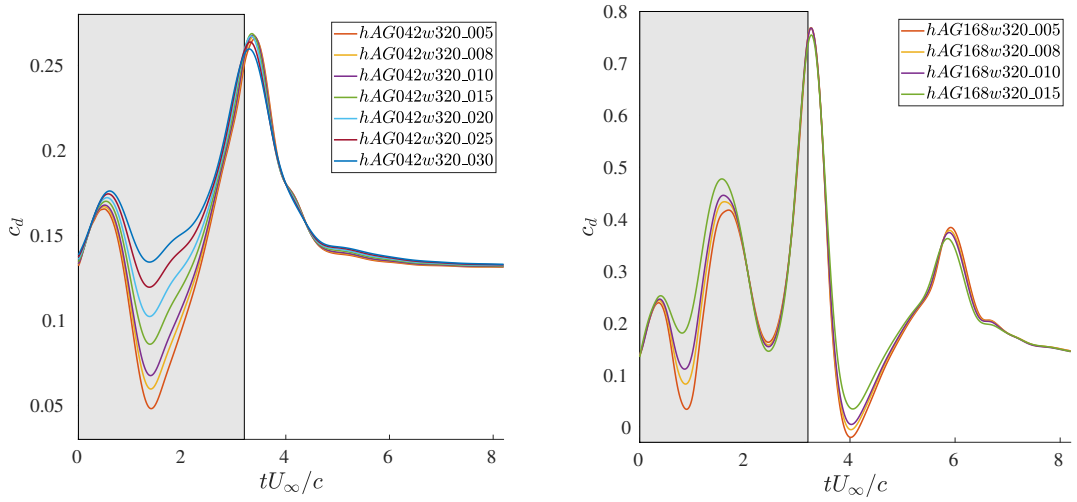

(a) (b)

Figure 3.5: Sensitivity to time step: c_d for (a) $GR = 0.42$ and (b) $GR = 1.68$

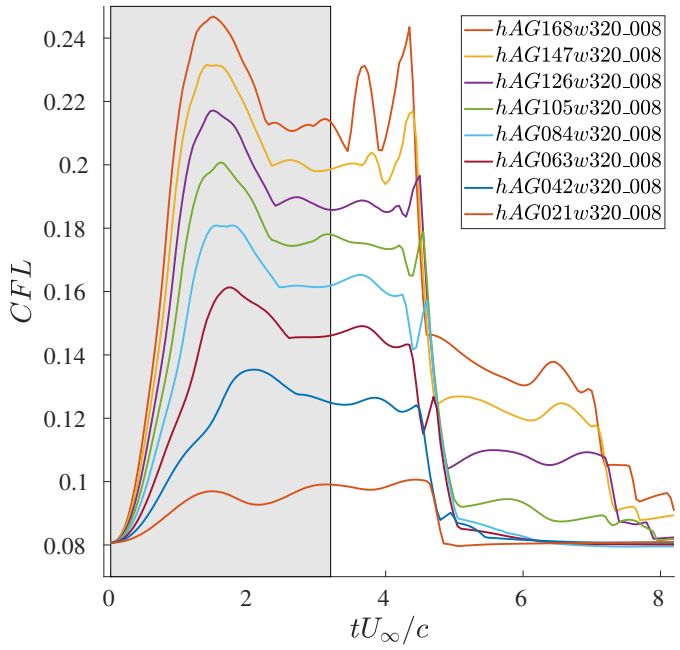

Figure 3.6: CFL of the main cases, gust ratio sweep for plunge maneuvers

3.2 Results and discussion

Regarding the aerodynamic coefficients, the lift is depicted in figures 3.7 and 3.8. Except for the case of very small gust ratios, the increment of lift is very significant. The sudden increase of lift while the airfoil enters the gust is mainly due to the emerging vortex from the leading edge, known as the leading edge vortex (LEV). As explained in the Introduction, the LEV plays a key role in unsteady low Re aerodynamics. As the gust ratio increases, the vortex is stronger and decreases the pressure on the upper surface, then the lift built is higher. After this sudden increase of lift, the LEV separates from the airfoil and it is shed downstream, explaining the decay of lift after its maximum value. Moreover, for relative medium to high gust ratios, there is a second episode of lift enhancement before the airfoil exits the gust, reaching the second maximum (lower in magnitude compared to the first one) approximately after exiting the gust. This effect will be better explained when analyzing a reference case in the next section. For very small gust ratios, it can be seen in figure 3.8 that rather than a second lift enhancement, there is a deficiency of lift.

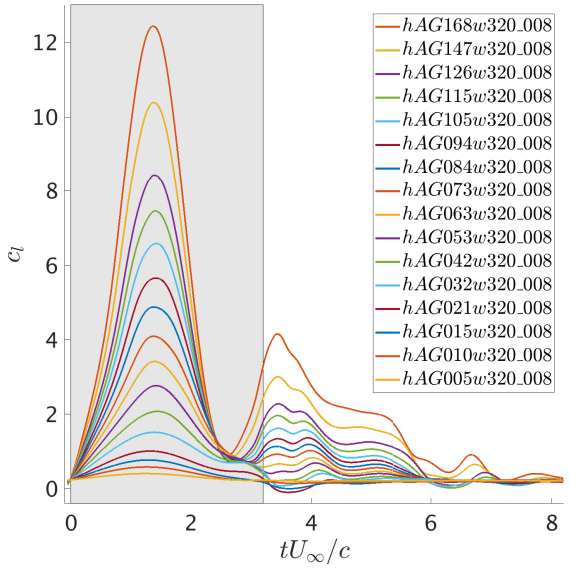

Figure 3.7: Lift coefficient of the plunging maneuvers, all gust ratios

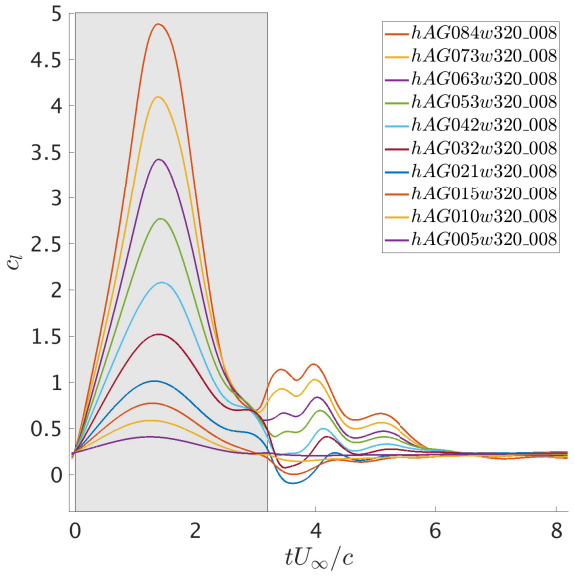

Figure 3.8: Lift coefficient of the plunging maneuvers, $GR < 0.84$

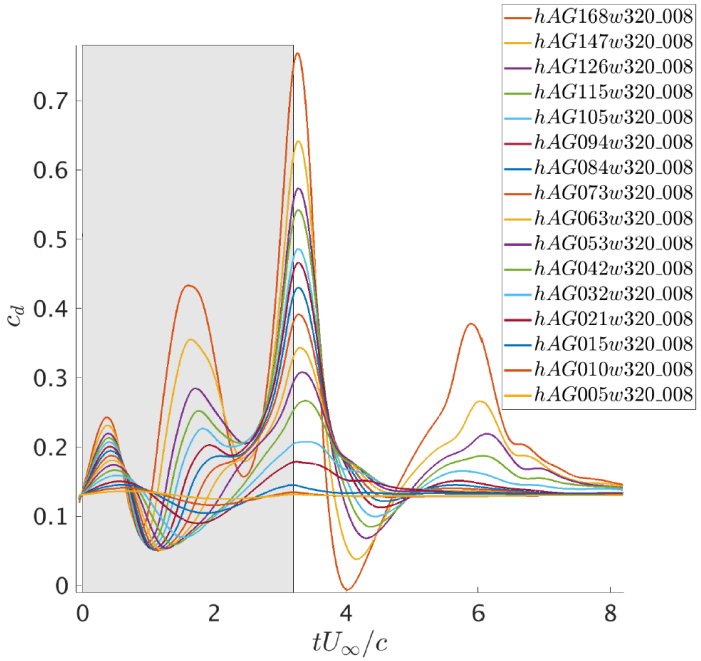

Figure 3.9: Drag coefficient of the plunging maneuvers

Concerning the drag coefficient depicted in figure 3.9, the behavior shows a higher

degree of complexity compared to the lift. Basically, the gust encounter implies non-symmetric oscillations of c_d with respect to the initial c_d value. The amplitude of these oscillations boost with gust ratio. The airfoil experiences several increases and decreases of drag with respect to the initial quasi-steady conditions. The biggest increase of drag occurs when the airfoil exits the gust. These behavior will be further explained for a reference case using vortex dynamics as well.

3.2.1 Analysis of a reference case

The reference case is the gust with GR=0.84. For that, this section focuses on case hAG084w320_008. The evolution of lift and drag coefficients is illustrated in figure 3.10. Figures 3.11 and 3.12 show vorticity fields of the domain near the airfoil at time instants indicated in Fig. 3.10 as red dot markers.

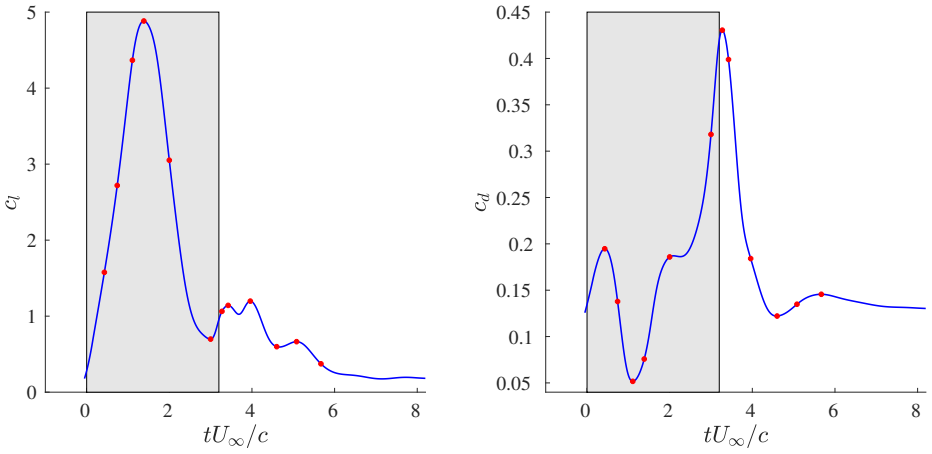

(a) (b)

Figure 3.10: Evolution of (a) lift and (b) drag coefficients for case hAG084w320_008. The red dots indicate the time instants at which vorticity fields are computed and shown below.

The first three vorticity snapshots during the heaving motion are prior to the maximum value of c_l which takes place at $\tilde{t} = 1.4$. During this time span, meanwhile the first LEV is developing, the flow on the upper surface of the airfoil experiences a trailing edge separation (negative vorticity, blue color).

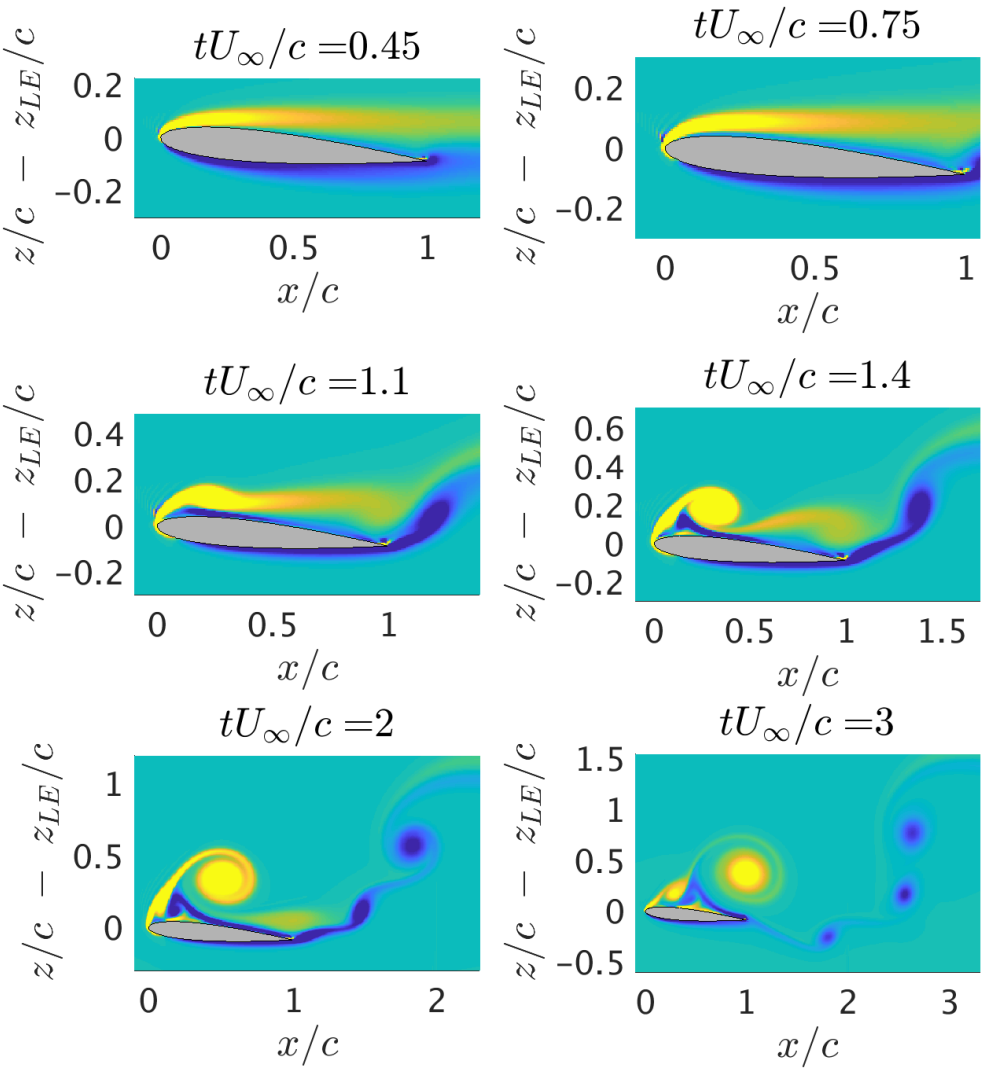

Figure 3.11: Vorticity fields $\omega_y c/U_\infty$ during the plunge maneuver, part 1. The yellow color represents the upper limit $\omega_y c/U_\infty = 5$ and the blue color represents the lower limit $\omega_y c/U_\infty = -5$.

The maximum lift and minimum drag are associated to the time instant $tU_\infty/c = 1.4$, where the first emerging LEV separates together with the development of another LEV, but weaker (see in Fig. 3.12 that the strongest turbulent structure is the first LEV among the other vortices). Although the first LEV has a great

prominence, it is also clear how other vortices are shed in the wake from the trailing edge. Figure 3.12 shows the shedding of the first LEV and the detachment of the second LEV from $tU_\infty/c = 3.25$ to $tU_\infty/c = 3.95$. At $tU_\infty c = 3.95$ we can observe the beginning of the shedding of a TEV, which ends up making a dipole with the first LEV.

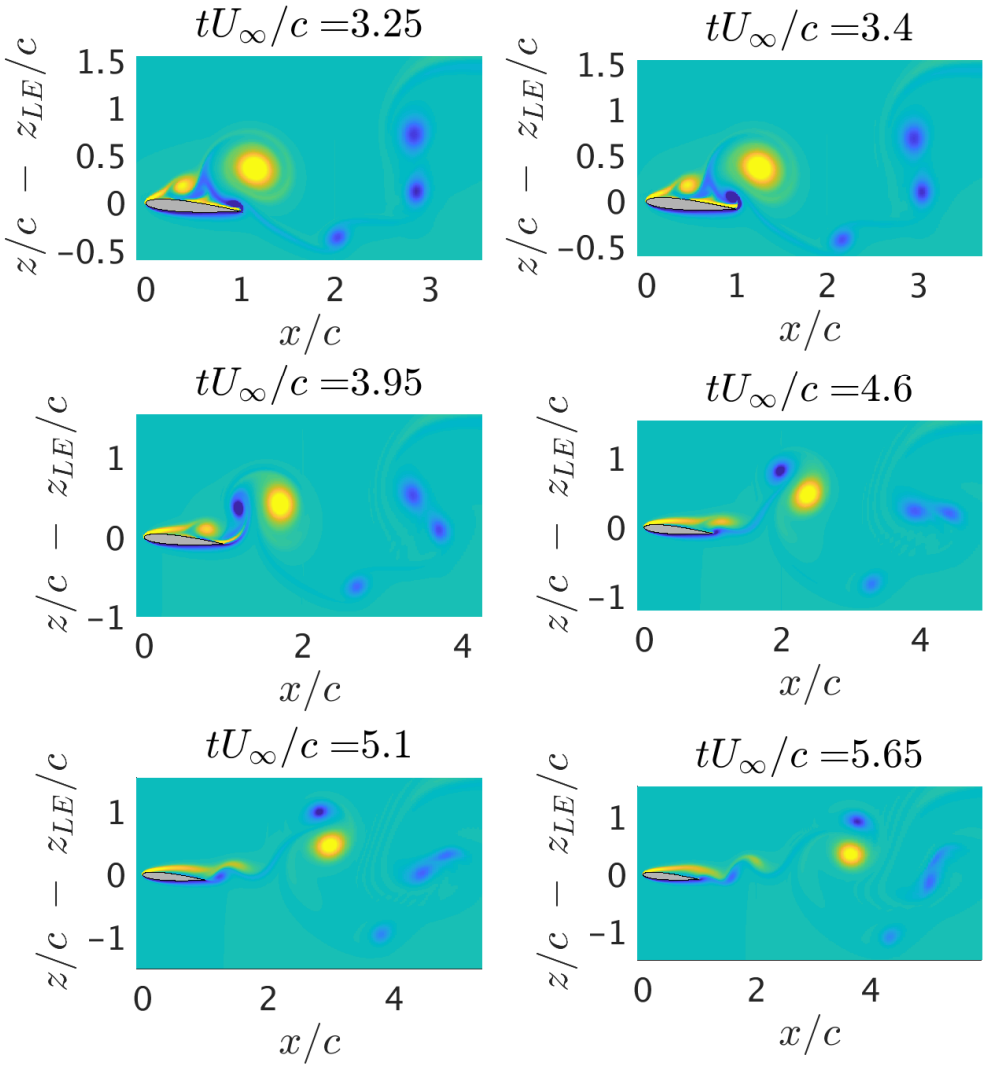

Figure 3.12: Vorticity fields $\omega_y c/U_\infty$ during the plunge maneuver, part 2. The yellow color represents the upper limit $\omega_y c/U_\infty = 5$ and the blue color represents the lower limit $\omega_y c/U_\infty = -5$.

After $tU_\infty/c = 1.4$, the lift starts to decay and the drag starts to increase because of the detachment of the first LEV (see also the high concentration of negative vorticity along the suction surface). It can be appreciated that near $tU_\infty/c = 3.2$, the lift to drag ratio may be near its minimum value during the gust. At this critical moment where the gust ends, the flow begins to re-develop to its initial state since now the freestream velocity is U_∞ again. However, this is not instantaneous, as we can see in the time histories of lift and drag after the gust. It is interesting the fact that even the airfoil has already exited the gust, there is a second lift-enhancement episode, but smaller in magnitude than the first one. This rebound is strongly related to the second LEV, but since this second vortex is weaker, the increase of lift is smaller this time.

The last three vorticity fields from Fig. 3.12 show how positive vorticity begins to predominate over the suction surface. It takes several chord lengths, almost ten, for the flow to reach quasi-steady conditions again.

3.2.2 Extension of the analysis to the database

After analyzing the gust with $GR = 0.84$, we present a parametric study of the sample of heaving cases. Figure 3.13 shows the evolution of the peak lift value during the gust and the evolution of the time instant at which it occurs. The peak lift value increases almost linearly with GR, while the time instant for the peak lift value remains around 1.4 convective times.

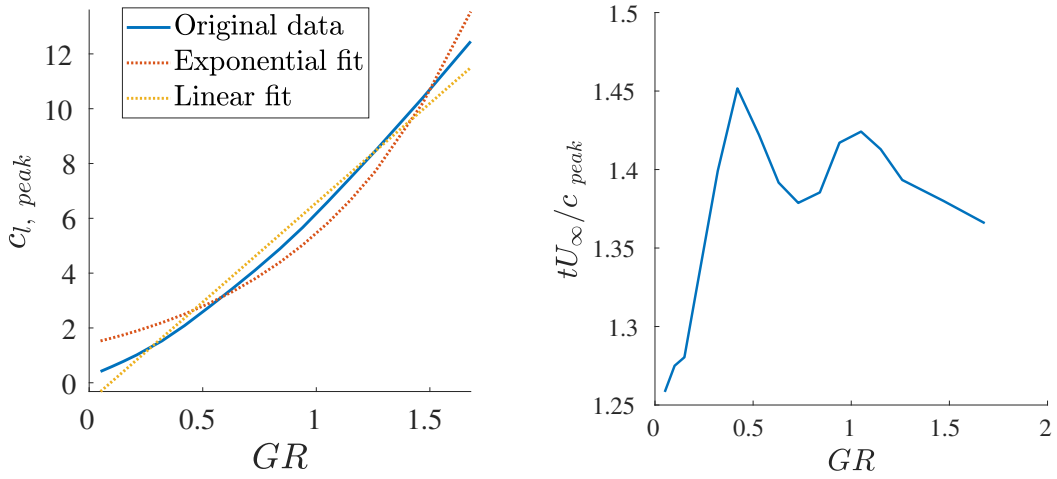

(a) (b)

Figure 3.13: Variation of (a) $c_{l,peak}$ with gust ratio and (b) $tU_\infty/c_{\ peak}$, plunge maneuvers

It was attempted to find the best fit to $c_{l,peak}$, as seen in Fig. 3.13 (a). The linear fit is the best candidate since the correlation is better and computationally it would be preferable to use a linear fit rather than an exponential one.

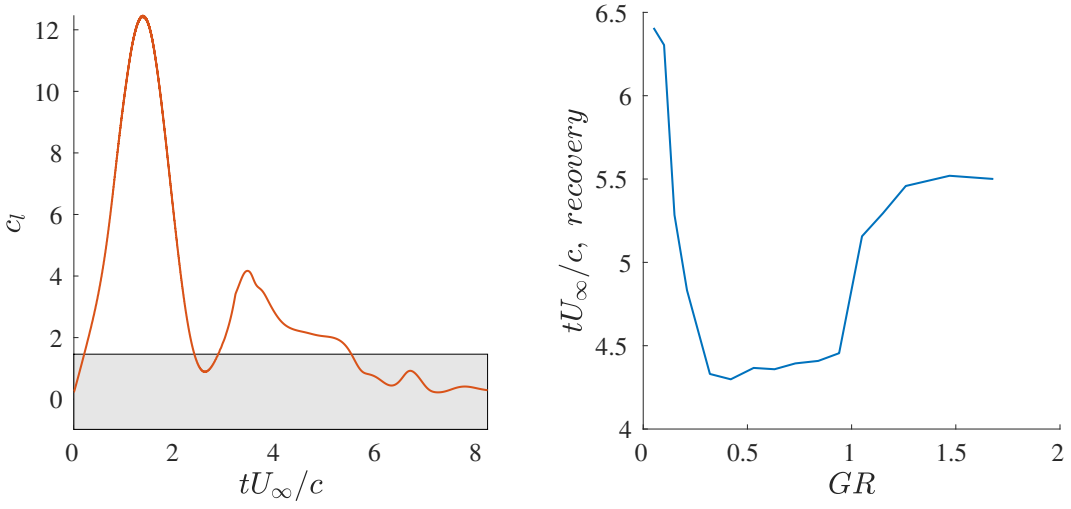

(a) (b)

Figure 3.14: (a) Illustration of the concept $t_{recovery}$ and (b) variation of $t_{recovery}$ with gust ratio, plunge maneuvers

Another variable to characterize the gusts may be $t_{recovery}$, i.e. the convective time from which the variation in lift coefficient around the initial value is less than 10% of its maximum value. This is better explained in figure 3.14(a) for case hAG168w320: the shadowed region is the zone where $|c_l| < 0.1c_{l,max}$. Hence, $t_{recovery}$ is the convective time instant at which the c_l signal enters the shadowed region and does not exit it anymore. According to figure 3.14(b), gusts with high gust ratio ($GR > 1$) usually take a longer time to recover the flow to a quasi-steady state compared to milder gusts ($GR \approx 0.4 - 0.5$). The reason why $t_{recovery}$ is high for gusts with very small gust ratio is because the boundaries of the shadowed region in figure 3.14(a) depend on the value of the peak lift. Since the peak lift value for very small gust ratio cases is very poor, the upper and lower tolerance boundaries for $|c_l| < 0.1c_{l,max}$ are very close to $c_l(\tilde{t} = 0)$, so it makes sense for small gust ratios to have a high $t_{recovery}$ according to this criterion for $t_{recovery}$ definition.

In addition, there is another figure which may characterize the gusts and it is the value of $\int_0^{8.2} \Delta c_l dt^*$. From an aeroelastic point of view, this integral quantifies the amount of energy and loads that the system, in this case a wing, may have to cope with. Figure 3.15 its similar to 3.13(a): as the gust ratio increases, the amount of energy put in the system increases linearly, in the same way as the peak lift value versus gust ratio.

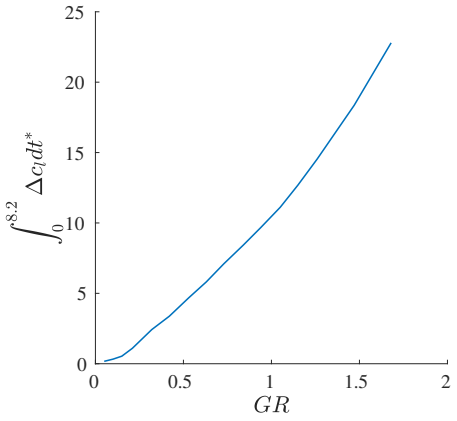

Figure 3.15: Quantification of the energy input during a gust

Chapter 4

Evaluation of alternative approaches to model gust encounters and comparison with results from the literature

4.1 Second approach for gust modelling: stationary jet, moving airfoil

After modeling the gusts as plunge maneuvers, there were sought other approaches for gust modelling to be implemented in the DNS solver. Taking advantage of the available tools within TUCAN, it was though to model the gusts as a moving airfoil who encounters a vertical jet. The reason for exploring new ways for gust modelling is to make more realistic approaches, and, if possible, cheaper computationally. For this second setup, the airfoil moves throughout a stagnant fluid and at some point it enters a stationary vertical jet whose velocity profile is given by Eq. (2.3), similarly to the experiments performed at the University of Maryland [4, 20].

One of the main differences between the jet gusts presented in this chapter and the plunge maneuvers is that the effective angle of attack is not constant anymore along the chord line, while the effective angle of attack did not vary chordwise during the previous heaving maneuvers. As desired, this new setup is more realistic and closer to the one presented in section 2.3, but also more expensive compared to the plunge maneuvers since it requires a larger mesh and a larger refined

zone, which turns into a lot of additional grid points.

4.1.1 Mesh choice and computational setup. Domain selection

For this second setup, the boundary and initial conditions are different. On the south boundary, it is imposed the following velocity profile

$$\frac{u_x}{U_\infty}(x,t) = 0$$

$$\frac{u_z}{U_\infty}(x,t) = \begin{cases} GRsin^2\left(\frac{\pi x/c}{w/c}\right) & -w/c < x/c < 0 \\ 0 & \text{otherwise} \end{cases}$$

For the north boundary, an advective boundary condition is set. For the east and west boundaries, a free-slip condition is imposed. Regarding the initial conditions, they are the following

$$\frac{u_x}{U_\infty}(x,z) = 0$$

$$\frac{u_z}{U_\infty}(x,z) = \begin{cases} GRsin^2\left(\frac{\pi x/c}{w/c}\right) & -w/c < x/c < 0 \\ 0 & \text{otherwise} \end{cases}$$

The Eulerian mesh is different. The airfoil moves with $u = U_\infty$ through a vertical jet with the desired "1-cosine" gust profile. This time the grid is larger chordwise because the airfoil must travel several chord lengths before entering the gust so that it is reached a developed flow around the airfoil prior the gust encounter. Once the leading edge enters the jet, it advances 9.2 chord lengths including the gust width. Note that the airfoil moves in the opposite direction of the conventional x direction and the jet gust is located within $\tilde{x} = [-w/c, 0]$ zone. During this motion, the vertical coordinate of the leading edge is always $z_{LE}/c = 0$. The grid is again cartesian, structured, staggered and non-uniform. Similarly to the mesh grid for plunge maneuvers, there is a refined zone and a relatively coarser one. The resolution is uniform chordwise with $d\tilde{x} = dx/c = 1/160$ for all cases, but it is not uniform in the z direction. The vertical stretching factor for the coarser zones in the z direction is 0.01.

In order to choose the size of the computational domain and to select a proper refined zone, different mesh configurations were done and they where tested for a

gust of $w/c = 3.20$ and $GR = 1.68$. This is done because it is desired to minimize the computational costs without losing accuracy in the results. The first trial has a domain with $x/c \in [-9.2, 20]$ and $z/c \in [-3, 7]$ (see case jAG168w320M1 in table 4.1). Note that the refined zone in the z direction also has a resolution of 160 grid points per chord lengths. The refined zone in the vertical direction is $z/c \in [-2, 4]$. Details about the remaining mesh configurations are shown in table 4.1. The nomenclature for these cases follows these rules: "j" stands for jet, "A" stands for geometric AoA=5°, "GXXX" denotes gust ratio of X.XX, "wXXX" means gust width w/c=X.XX and "MX" indicates the mesh trial number X.

Case	**x/c domain**	**z/c domain**	**Refined z/c zone**	**Grid points (millions)**	**CFL_0**
jAG168w320M1	[-9.2,20]	[-3,7]	[-2,4]	5.75	0.380
jAG168w320M2	[-9.2,15]	[-2,6]	[-1,4]	4.02	0.190
jAG168w320M3	[-9.2,15]	[-3,8]	[-1,6]	5.45	0.095
jAG168w320M4	[-9.2,15]	[-3,10]	[-2,7]	6.63	0.095
jAG168w320M5	[-9.2,15]	[-2,6]	[-1,4]	4.02	0.095

Table 4.1: Mesh configurations for jet gust simulations

An example of the fluid domain and the airfoil's motion of this second setup is depicted in figure 4.1:

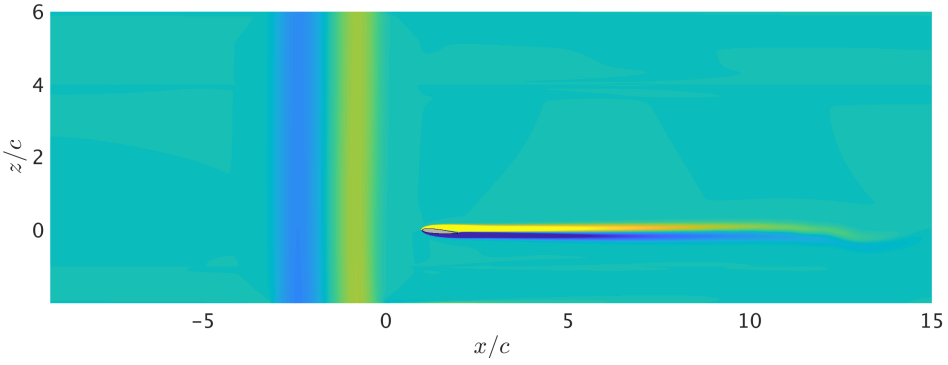

Figure 4.1: Fluid domain of the second setup, cases jAG168w320M2/M5

With case jAG168w320M1 it was seen that it is enough to travel 15 chord lengths instead of 20 before entering the gust because the airfoil also achieves quasi-steady conditions (convergence of force values) in a motion of 15 chord lengths before the gust (see figure 4.2). Then, it was decided to shorten the x domain to $x/c \in$

$[-9.2, 15]$ for the other test cases. In order to examine the variations of the aerodynamic coefficients in figure 4.4, case jAG168w320M1 is discarded because the CFL during the gust encounter (see figure 4.3) is higher than 0.5 during the gust.

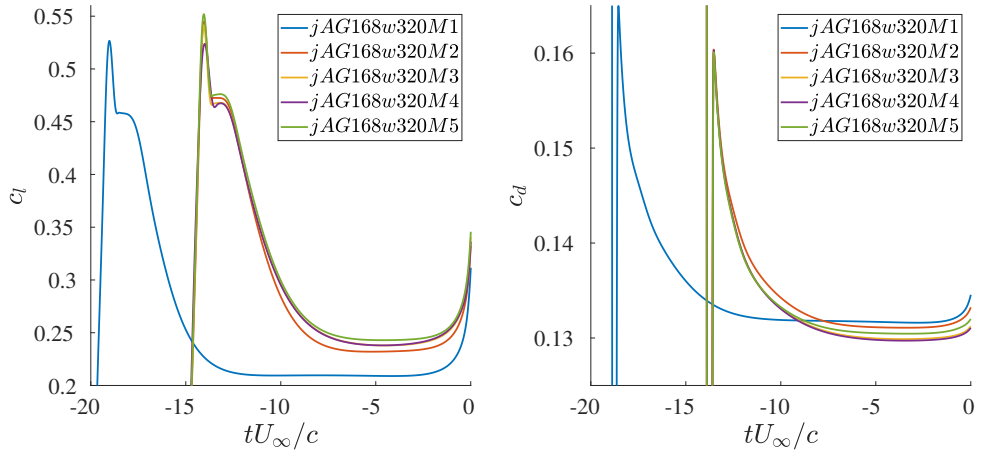

Figure 4.2: Convergence to quasi-steady conditions, mesh testings for jet gusts

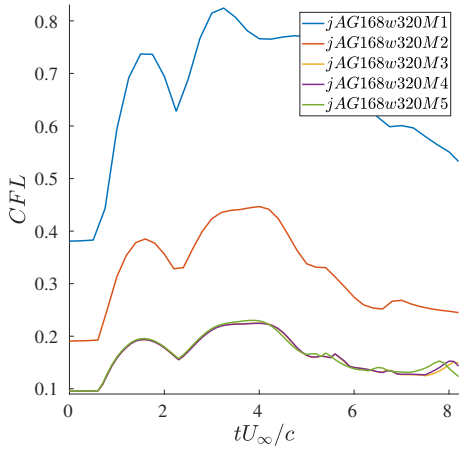

Figure 4.3: Time history of CFL for test cases in table 4.1

It is observed in figure 4.4 that cases jAG168w320M3 and jAG168w320M4 have very similar, almost identical, results even though the mesh grid for case jAG168w320M4 has a bigger refined zone and a larger domain. Then, now we must choose between

cases jAG168w320M2, jAG168w320M3 and jAG168w320M5 in order to preserve an acceptable mesh for jet gust simulations. Case jAG168w320M5 has the same mesh grid as case jAG168w320M2, but with a smaller time step. We are aware of the sensitivity of TUCAN to the time step, so we prefer to use a time step as small as possible for the DNS. Since case jAG168w320M5 has less grid points and the results are very similar compared to the ones from case jAG168w320M3 which has a finer and bigger mesh, it was considered to take the mesh for case jAG168w320M5 as the definitive one for jet gust simulations. One may choose the mesh from case jAG168w320M4, whose domain is larger and has a larger refined zone, but the results do not differ significantly even though were are talking about a difference of 2.6 million grid points for a similar domain. Computational power and the time that the simulations take to be completed are a current limitation of DNSs, so that this is why we prefer to go on with the mesh from case jAG168w320M5.

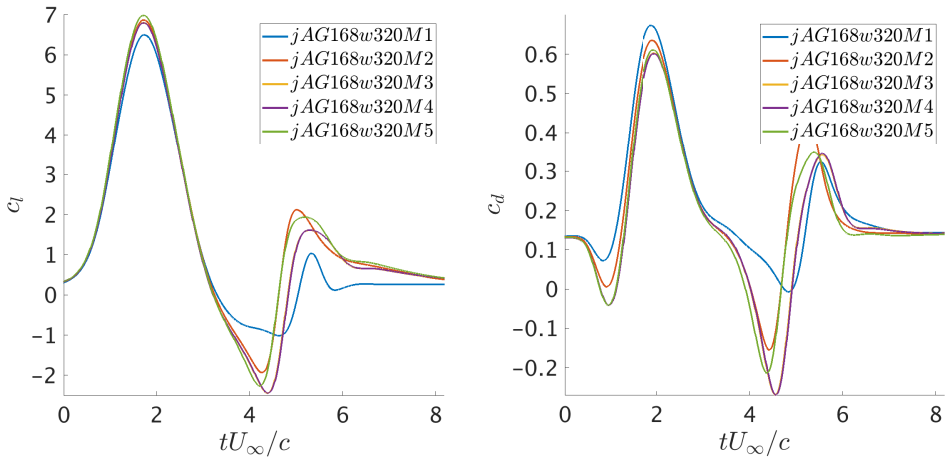

Figure 4.4: Evolution of aerodynamic coefficients during a gust encounter for test cases in table 4.1

In order to make sure that the airfoil sees the desired vertical velocity while it enters the jet, a sample window is taken from the domain to analyze it. The domain of this sample window is $\tilde{x} \in [-w/c, 0]$, $\tilde{z} \in [-1, 1]$, which is shown in Fig. 4.5 for case jAG084w320. The analysis of this sample window consists on calculating the mean vertical velocity u_z value at each constant x coordinate. Once this is done, the profile of the mean u_z is compared to the desired one (1-cosine gust) and with $u_z(z = 0)$ because $z_{LE} = 0\ \forall t$. This is shown on figures 4.6 (a), 4.6 (b) and 4.7 for all three cases. Hence, referring to the velocity profile of the jet, it is clear that gust is properly set up.

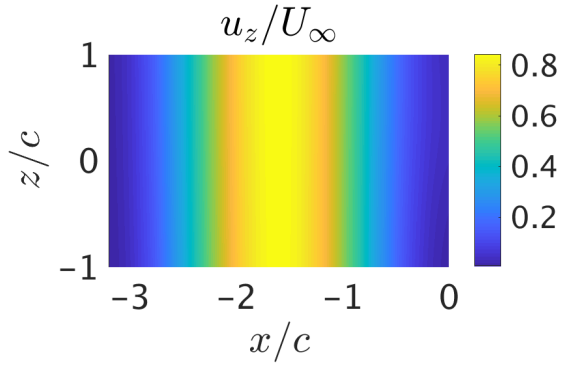

Figure 4.5: Sample window for analyzing the vertical velocity profile within the jet, case jAG084w320

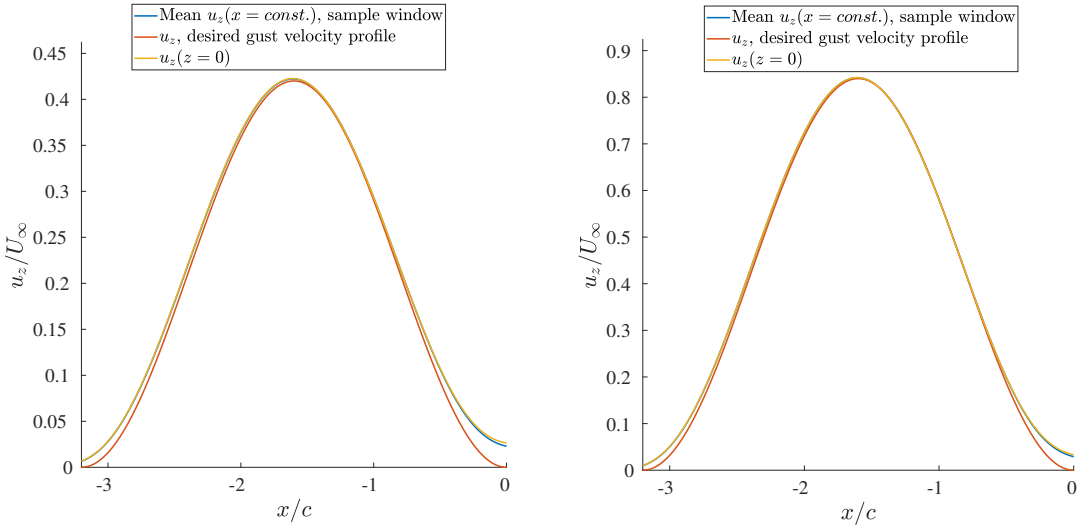

(a) (b)

Figure 4.6: Analysis of the vertical velocity within the jet, cases (a) jAG042w320 and (b) jAG084w320

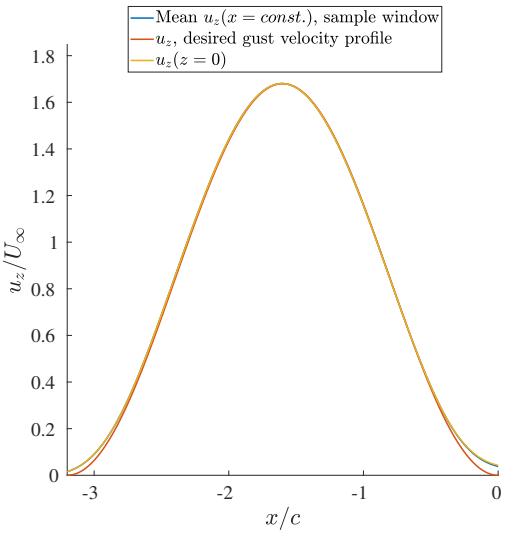

Figure 4.7: Analysis of the vertical velocity within the jet, case jAG168w320

4.1.2 Results and discussion

For the jet gusts, the non-dimensional set of parameters which define the problem is composed of $Re,\ GR,\ w/c,\ \alpha_0$. The Reynolds number is $Re = 1000$, the gust width is $w/c = 3.2$ and the geometric AoA is $\alpha_0 = 5^o$. The cases for this setup are resumed in table (4.2).

Case	Re	α_0	w/c	GR
jAG042w320	1000	5^o	3.20	0.42
jAG084w320	1000	5^o	3.20	0.84
jAG168w320	1000	5^o	3.20	1.68

Table 4.2: Cases for the second setup

Figure 4.8 shows the evolution of the aerodynamic coefficients during the gust encounter. There are notable differences compared to the results presented for plunge maneuvers (see Figs. 3.7, 3.9). The shape of the lift curves are a little similar: due to the appearance of a LEV, there is a considerable lift enhancement followed by a decay until the airfoil exits the gust, followed by a second lift peak smaller in magnitude. This time, the peak lift values for a gust with identical parameters are smaller compared to the results for heaving cases. In addition, taking into account the evolution of lift of case jAG168w320, it seems that for large gust

ratios the flow takes a longer time to restore to its previous quasi steady conditions. Regarding the drag time histories, the behavior is quite different this time, especially if we compare mild and strong gusts. What is surprising is that the drag starts to decrease instead of increase as the LEV emerges. The evolution of the drag coefficient in this case for GR=1.68 is similar to the one for the heaving case in terms of the oscillations about the initial drag coefficient.

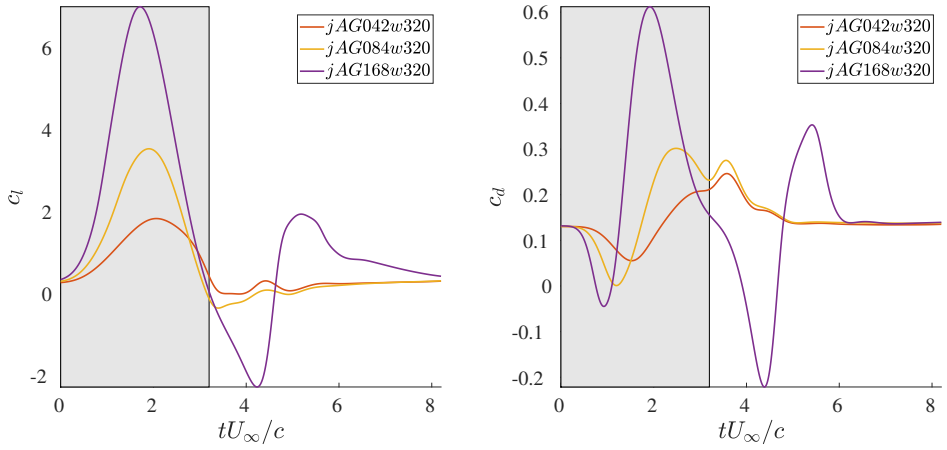

Figure 4.8: Evolution of lift and drag coefficients of jet gusts

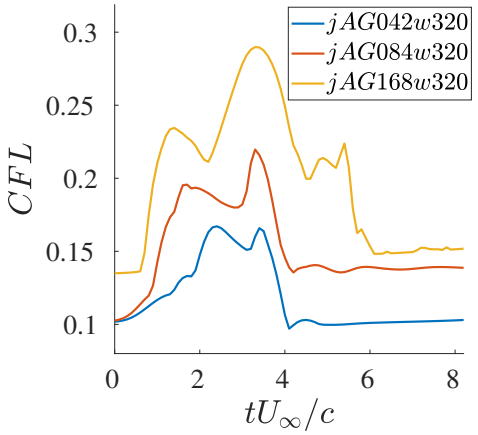

Figure 4.9: Evolution of CFL of jet gusts

Concerning the time step chosen for the cases of jet gusts, it was small enough so that $CFL < 0.5$ for all jet gust simulations (see Fig. 4.9).

Figure 4.10 shows the results from different setups for the reference gust case (GR=0.84). Analogous to case hAG084w320_008, the vorticity fields shown in Fig. 4.11 for case jAG084w320 are captured at time instants marked with red dots in Fig. 4.10.

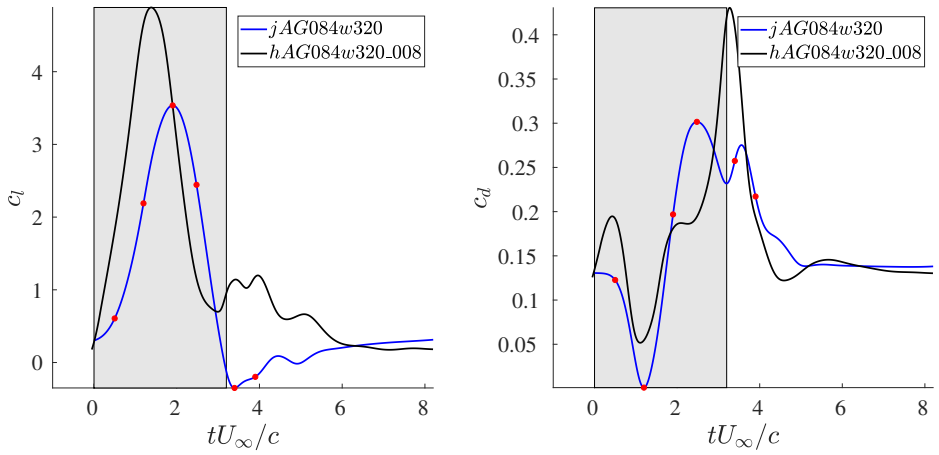

Figure 4.10: Time histories for aerodynamic coefficients during the gust encounter, case jAG084w320. The red dots indicate the time instants at which vorticity fields are computed and shown below

As previously pointed out, there are some significant differences between the two setups, i.e. the plunge maneuver and the jet gust. Regarding the lift, there is some qualitative similarity between time histories of a same gust (see figure 4.10). On the other hand, the drag time histories are both different qualitatively and quantitatively. Concerning the lift, there is a quantitative difference such as the magnitude and time instant of the first peak lift. For the jet gust configuration, the formation of the first LEV is at a slower rate and it is weaker, i.e. it does not perturb the pressure distribution on the suction surface as strong as in the case of the plunging maneuver. In both setups, as the first LEV starts to be shed into the wake, the lift starts to decay as the drag continues to increase. Concerning the notable TEV that appears when the LE exits the jet gust, this may be responsible for part of the differences between the heaving and jet results. The formation of this TEV during the jet gust is in some way expected since the rear part of the airfoil sees a vertical incoming flow while the LE is out of the gust region.

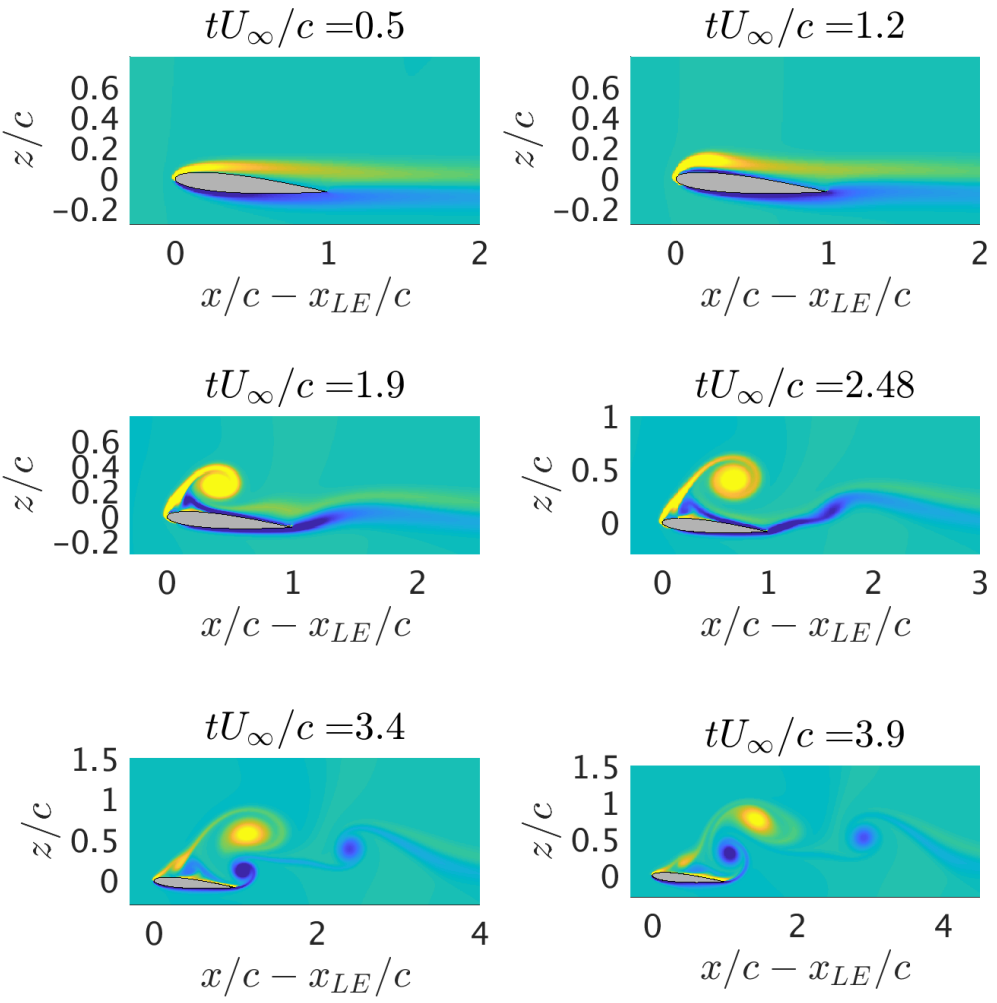

Figure 4.11: Vorticity fields $\omega_y c/U_\infty$ case jAG084w320

4.2 Comparison with similar experiments from the literature

Recently, Perrotta and Jones [20] performed several gust-encounter experiments at the University of Maryland. The experiments consisted on studying the aerodynamic forces on a flat plate of aspect ratio 4 while it goes through a jet gust

with '1-cosine' profile. Although they mention the gust width was $w/c = 3.18$, their results (see blue line in figure 4.12(a)) seem to be for a wider gust. This last fact occurs because they use a low-profile flow straightener to clear the streamwise waving fluctuations of the jet; in other words, they use a screen in order to make sure the flow is uniform within the vertical jet. The fluid medium is water instead of air and PIV is used to compute flow magnitudes.

Experiments in [20] are done with a wing of aspect ratio 4. We can apply a transformation to the wing results to get airfoil-equivalent results by multiplying the wing aerodynamic coefficients by the following factor:

$$\frac{2 + AR}{AR}$$

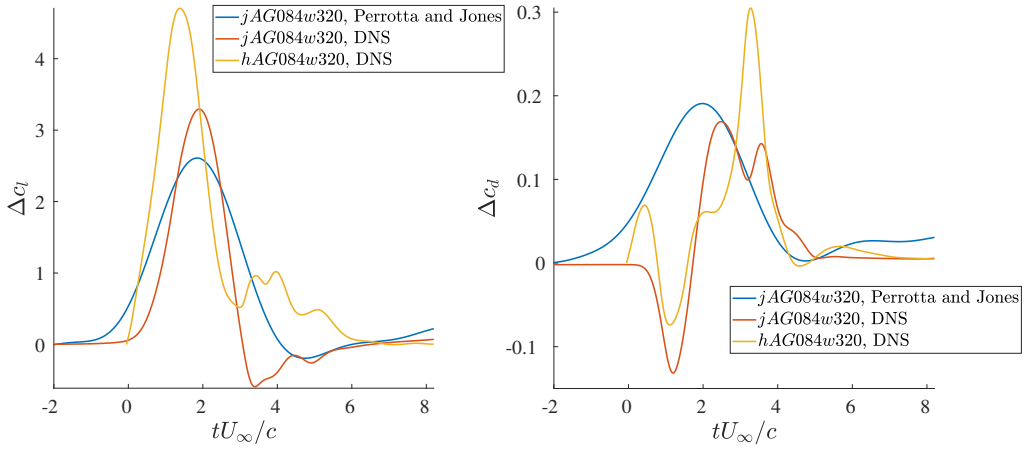

(a) (b)

Figure 4.12: Comparison of results with experiments done by Perrotta and Jones [20]

The comparison made in figure 4.12 between the results of this thesis and those from [20] is for a GR=0.84 gust is done in terms of increments of aerodynamic coefficients. Concerning the lift, there is some qualitative similarity between the different time histories, i.e. the lift increases due to LEV appearance and then it starts to decay after its peak value occurring nearly at the same moment, returning to the initial quasi-steady conditions several convective times after exiting the gust. The peak lift from [20] has a low magnitude, similar to case jAG084w320.

The lift history from the heaving DNS case does not resemble too much the jet gust DNS or the results from [20], so plunge maneuvers may overestimate the lift. Regarding the drag, all three cases bring different behaviors. While the DNS cases predict a thrusting force which lowers the drag while the LEV emerges, the drag force from the experiment increases from the first time instant when the flat plate enters the gust.

The differences shown above are in some way expected because the blue line curves in figure 4.12 are experiments done at $Re = 20.000$, while the DNS results from this project are done at $Re = 1000$. Therefore, this big difference in the nature of the flow regime is one reason for different results since three-dimensional effects are expected to appear in those experiments. Although the DNS is done at a Reynolds number low enough so that 3D effects are expected to be absent, the 2D DNS is not capable of capturing the wing tip vortices, which are very likely to be present in the flat plate experiment.

Despite these differences, Perrotta and Jones [20] observed that the main lift enhancement mechanism is the LEV and the evolution of the lift coefficient over time is coherent with the one found in the DNS. They also observed the presence of the local minimum of lift that occurs after exiting the gust. In section 4.1.2 we affirmed that this phenomenon is very bound to the TEV that appears when the airfoil exits the jet gust, and both Perrotta and Jones are sure about that.

4.3 Proposal of a third approach: stationary airfoil, travelling jet

This section presents a new approach for modelling gust encounters within TUCAN. The main purpose for looking for other approaches is to minimize the computational costs, bring the computational setup to a more realistic one and ease the implementation in a future 3D DNS case.

The idea of this new approach is to keep the airfoil motionless and simulate the gust encounter by playing with the free-stream velocity. The immersed boundary method will be used to impose the non-slip boundary condition and to compute the forces on the airfoil. Using a stationary airfoil and a travelling jet decreases the computational cost without loosing its realistic component. Moreover, this approach is more affordable for implementing in 3D setups compared to the previous approach (jet gust, moving airfoil, stationary jet) because the second approach of this thesis, implemented in a 3D setup, would have a very high cost.

For the purpose of this new approach, a volumetric force term will be introduced in the incompressible Navier-Stokes momentum equation:

$$\frac{\partial u_i}{\partial t} + u_j \frac{\partial u_i}{\partial x_j} = -\frac{1}{\rho}\frac{\partial p}{\partial x_i} + \nu \frac{\partial^2 u_i}{\partial x_i^2} + f_i \tag{4.1}$$

where x_i is the cartesian coordinate, u_i is the velocity component, p is the pressure, ρ is the fluid density and ν is the kinematic viscosity of the fluid.

The continuity equations must be fulfilled as well:

$$\frac{\partial u_i}{\partial x_i} = 0 \tag{4.2}$$

The free-stream velocity will have a component $u_x = U_\infty$ and $u_z = w(x,t)$.

The continuity equation reads:

$$\nabla \cdot \vec{u} = \frac{\partial u_x}{\partial x} + \frac{\partial u_z}{\partial z} = 0 + 0 = 0 \tag{4.3}$$

The momentum equation yields two scalar equations:

$$\frac{\partial u_x}{\partial t} + u_z \frac{\partial u_x}{\partial z} = -\frac{1}{\rho}\frac{\partial p}{\partial x} + \nu \frac{\partial^2 u_x}{\partial x^2} + f_x \Rightarrow 0 = -\frac{1}{\rho}\frac{\partial p}{\partial x} + f_x \tag{4.4}$$

$$\frac{\partial u_z}{\partial t} + u_x \frac{\partial u_z}{\partial x} = -\frac{1}{\rho}\frac{\partial p}{\partial z} + \nu \frac{\partial^2 u_z}{\partial z^2} + f_z \Rightarrow \frac{\partial w}{\partial t} + U_\infty \frac{\partial w}{\partial x} = -\frac{1}{\rho}\frac{\partial p}{\partial z} + f_z = g_w(x,t) \tag{4.5}$$

where $g_w(x,t)$ is a known function once the moving gust profile u_z is known, so g_w will be treated as known. Note that f_x and f_z do not denote partial derivatives, they simply stand for x and z components of the volumetric force components.

Therefore, the momentum equation resumes to

$$0 = -\frac{1}{\rho}\frac{\partial p}{\partial x} + f_x \tag{4.6}$$

$$g_w(x,t) = -\frac{1}{\rho}\frac{\partial p}{\partial z} + f_z \tag{4.7}$$

Considering equation (4.7), the left handed-side is a function of x and t only, so we can impose that both terms of the right handed-side are also functions of x an

t. Then, it turns out that $\partial p/\partial z$ is only a function of x and t and the pressure function would be

$$p(x,z,t) = zA(x,t) + B(x,t) \Rightarrow \frac{\partial p}{\partial z} = A(x,t) \tag{4.8}$$

where A and B are unknown functions.

According to (4.8), the volumetric-force terms in the momentum equation would be:

$$f_x = \frac{1}{\rho}\frac{\partial p}{\partial x} = \frac{1}{\rho}\left[z\frac{\partial A}{\partial x} + \frac{\partial B}{\partial x}\right] \tag{4.9}$$

$$f_z = g_w + \frac{1}{\rho}\frac{\partial p}{\partial z} = g_w + \frac{1}{\rho}A \tag{4.10}$$

Taking the divergence of the momentum equation, it yields the following Poisson equation:

$$\Delta p = \rho \nabla \cdot \vec{f} \tag{4.11}$$

Using the expressions for the volumetric-force terms, the Poisson equation for the pressure becomes

$$\Delta p = \rho\left(\frac{\partial f_x}{\partial x} + \frac{\partial f_z}{\partial z}\right) = z\frac{\partial^2 A}{\partial x^2} + \frac{\partial^2 B}{\partial x^2} \tag{4.12}$$

The next step for simplifying the approach is assuming that the divergence of the volumetric-force is zero, yielding $\partial^2 A/\partial x^2 = 0$ and $\partial^2 B/\partial x^2 = 0$. Then, the Poisson equation for the pressure becomes a Laplace equation for p which satisfies equation (4.8).

A first solution to the problem is the trivial solution $p = 0$ which satisfies all the previous equations, leading to the following expressions for the volumetric-force terms:

$$f_x = 0 \tag{4.13}$$

$$f_z = g_w = \frac{\partial w}{\partial t} + U_\infty \frac{\partial w}{\partial x} \tag{4.14}$$

With this solution, the expression for $\vec{f}$ does not depend on initial and boundary conditions; it only depends on the desired gust field. If we do not face numerical problems, a simulation that implements this forcing term yields the desired velocity and pressure values in the free-stream. Of course, once we put inside our domain an airfoil, the velocity and the pressure fields change.

Chapter 5

Prediction of aerodynamics forces on airfoil during gust encounters

As mentioned in the Introduction and Chapter 2, direct numerical simulations require a considerable computational cost and time for solving the N-S equations accurately. The use of reduced-order models vanishes the need for using DNS to get similar results with a very low computational cost, and a lot faster. The drawback of these models is that they may work very well for certain Re range or very specific gusts, i.e. a model made for a particular gust at a certain Re number may deteriorate if we change the Re number or the gust profile. Predictive models are a key component for designing a flight control systems for a MAV covering a large gust envelope. As mentioned in the Introduction, current MAV's size, weight and dimensions make it impossible for having a N-S solver within the electronic control block of the vehicle, so the development of a reduced order model is needed for further implementation on the dynamic equations of an MAV. Although the predictive models may work satisfactory, the user must be aware that they are strictly dependent on a big set of assumption and they do not reflect the reality.

The goal of Chapter 5 is to show the performance of different force-predictive models during a gust encounter, imposing a certain velocity profile of the gust, which is known a priori. The analysis focuses on the increment of lift Δc_l, which is the force always perpendicular to the far-field free stream velocity U_∞ all the time.

As explained in Chapter 2, this project we elaborate two simple models: a semi-empirical quasi-steady one and an unsteady one using a convolution approach with Kussner and Wagner functions.

5.1 Results and discussion

In order to evaluate the performance of the models, Figure 5.1 shows different lift predictions using the quasi-steady model and the indicial one, for two different gusts: a mild one with GR=0.42 and the most intense which has a GR=1.68.

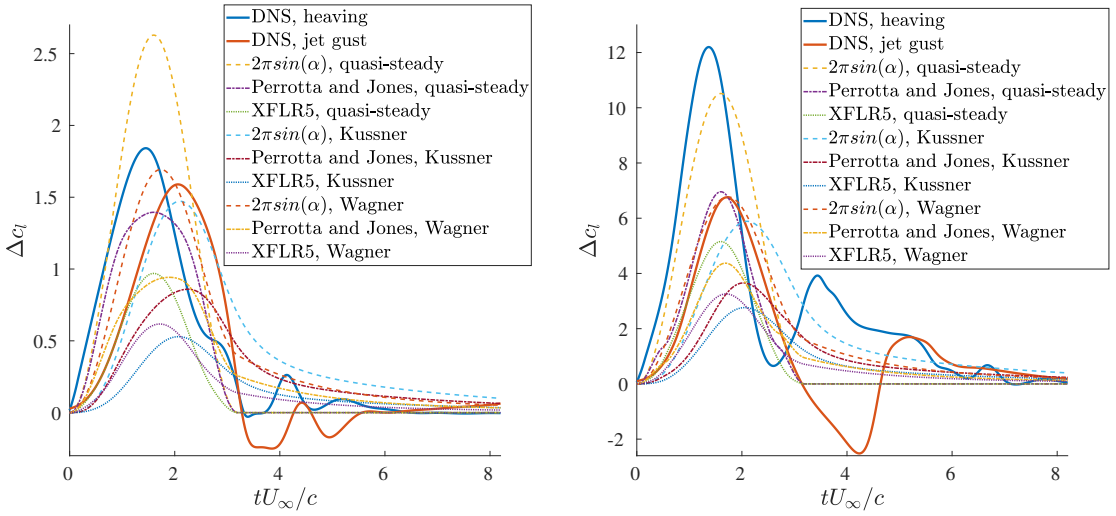

Figure 5.1: Different lift predictive models for (a) GR=0.42 and (b) GR=1.68

Concerning the quasi-steady model, it does not capture any recovery process after the airfoil exits the gust. Nevertheless, the indicial response predicts a recovery process after the gust, which is a good aspect since we are interested in lift prediction after the gust as well. Another issue of interest is the prediction of the lift peak and the shape of the DNS curves. In addition, it is clear that for all indicial responses the Wagner's function yields a bigger estimation compared to Kussner's function.

As it can be seen in figure 5.1(a), the $2\pi sin(\alpha)$ with Wagner's function convolution is a good candidate to predict the blue curve which stands for the heaving DNS. Although the '$2\pi sin(\alpha)$, Wagner' curve is close to the heaving gust DNS, the '$2\pi sin(\alpha)$, Kussner' curve works better with the second DNS version (jet) if we are more interested in matching the peak lift of the jet gust DNS.

The thin airfoil theory combined with the quasi-steady model brings the highest values of lift, for all gust ratios. This works well for high gust ratios because the yellow dashed curve is the closest one to the heaving DNS. The reason why the

potential theory outputs the highest results is because it does not capture flow detachment, so it assigns the highest lift coefficient at high angles of attack where the real value for c_l is smaller for sure. However, for small gust ratios, the indicial responses using thin airfoil theory data work better than the quasi-steady model.

Concerning the other data inputs, i.e. data from Perrotta and Jones experiments and XFLR5, the prediction is more deficient: both quasi-steady and unsteady models using this data underestimate the peak lift value and the shape of the DNS curve is not properly matched.

Up to now it looks like the thin airfoil theory is the best option of input data for the models. This fact was very unexpected since potential theory does not look like to be a proper candidate to play within the field of unsteady low-Re aerodynamics. As mentioned above, the tricky thing about potential theory is that although it does not take into account viscous and thickness effects, including the LEV's influence, it offers high lift values for high angles of attack where the flow separation is significant. However, in spite of the flow separation that occurs during the gust encounters, the emerging of the LEV observed in the DNS and in the experiments makes sure the lift increases to a greater extent.

As seen in figure 5.1, the indicial responses usually do not reach DNS values prior to the peak lift and they overestimate the lift after this first peak. Kussner's and Wagner's functions are potential models and they assume Kelvin's circulation theorem which states that the material derivative of the circulation on a contour enclosing the airfoil and the wake is zero. In other words, these functions assume a compensation of circulation between the wake and the circulation around the airfoil's surface. However, in the context of this study, this idea does not hold. Unsteady potential models such as Kussner's and Wagner's functions do not capture the LEV effect and also they do not take into account flow separation; that is why the lift from the DNS signals increases at a bigger rate when the airfoil enters the gust and the LEV starts to emerge and it is also the cause for lift overestimation of the unsteady model after the peak lift instant.

Before closing the analysis of the different predictive models, it was considered to study the prediction of the parameters treated in section 3.2.2 comparing them with the heaving DNS results: the peak lift value, the time instant of the peak lift value, the so-called $\tilde{t}_{recovery}$ and the area under the lift curve.

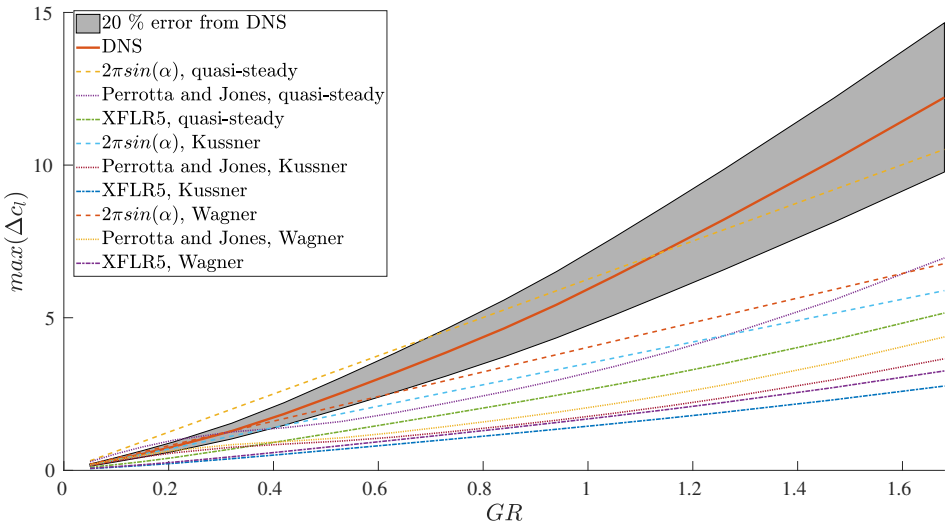

Figure 5.2: Prediction of the peak lift value

Figures 5.2 and 5.3 show the predictive capability of the models for estimating the peak lift value. This is the reason why it was needed a big database for plunge maneuvers. The shadowed regions represent the zone with a 20% error from the DNS value. In both plots we can see that for small to medium gust ratios, the best predictive model is the indicial one using Wagner's function and the $2\pi sin(\alpha)$ lift curve. This fact is expected since the Wagner's function is designed for instantaneous changes of the geometric angle of attack and, on the other hand, during the plunge maneuvers the effective angle of attack does not vary chordwise and it changes as we heave the airfoil downwards, so in principle there is expected a good performance of than model for plunge maneuvers of small to medium gust ratios. For medium to high gust ratio, the thin airfoil theory combined with the semi-empirical models works better than any other model. What is interesting about figure 5.3 is that for high gust ratios there is a scaling factor between the real DNS value and the value provided by models using data from Perrotta & Jones and XFLR5. The XFLR5 curves are the most flat ones. Then, if we tune the XFLR5 models multiplying by a factor of, e.g. 2, we would fit the models using XFLR5 data within the shadowed region.

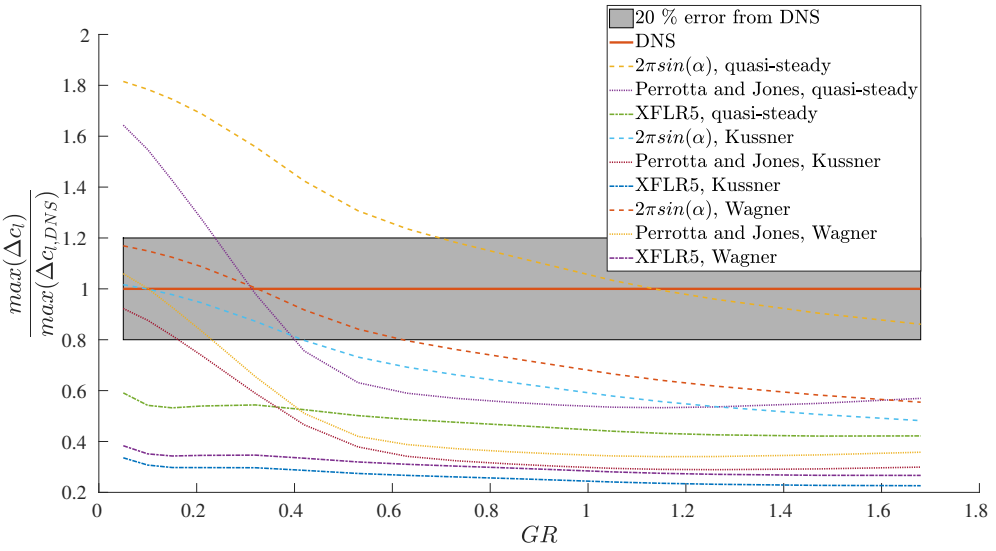

Figure 5.3: Prediction of peak lift values with respect to the heaving simulations

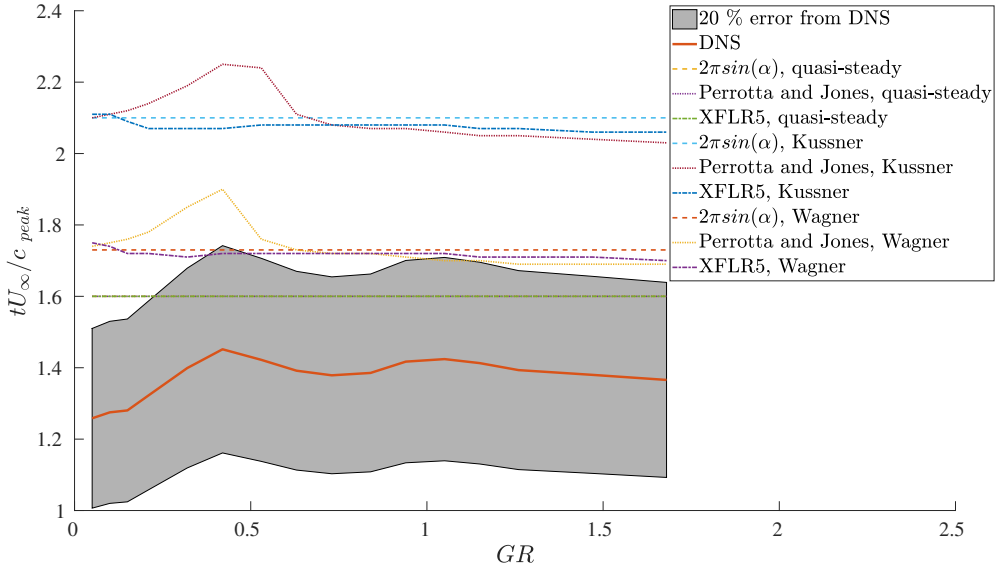

Figure 5.4: Prediction of the time instant at which the peak lift value occurs

Regarding the prediction of the convective time at which the peak lift occurs, figure 5.4 shows that the best option is the thin airfoil theory combined with the semi-empirical model, which predicts the peak lift at the middle of the gust. This

make sense thanks to the '1-cosine' profile gust and because the thin airfoil theory provides the highest lift value for the highest effective angle of attack, which occurs at the middle of the gust, in this case at $\tilde{t} = 1.6$. Concerning the models combining the thin airfoil theory and the indicial response, they predict the peak lift at the same time instant no matter the gust ratio. This last fact is because expression (2.11) is linear with GR if we use the potential theory as input data. In addition to the potential and semi-empirical model, the thin airfoil theory combined with the convolution integral predicts the best time instant for the peak lift if we want to use an unsteady model in order to capture recovery effects after the gust.

The prediction of the $\tilde{t}_{recovery}$ parameter is illustrated in figure 5.5. Obviously this makes sense only for the indicial responses since the quasi steady models do not provide any lift relaxation process after the gust. Even though the 'XFLR5, Wagner' curve may be the best option, one may take the option of potential theory and Wagner since this model behaves adequately as it has been discussed above.

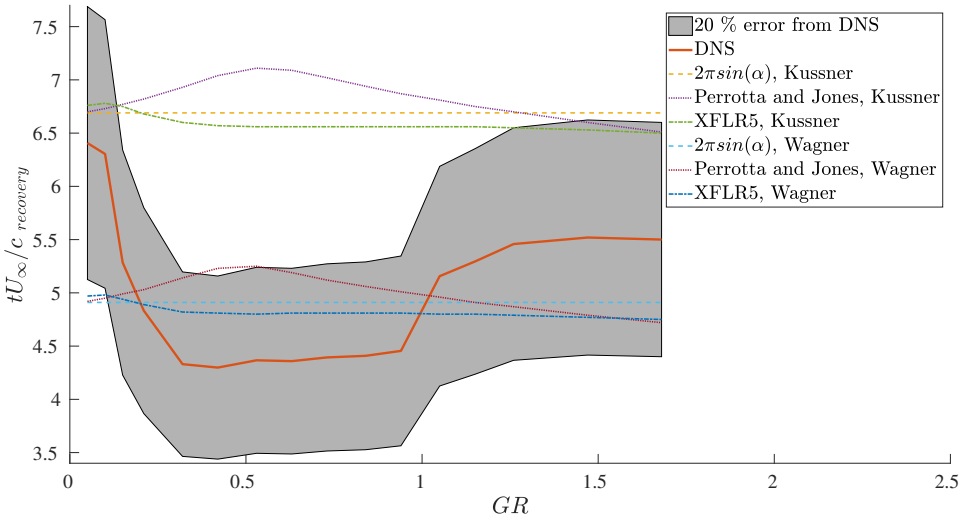

Figure 5.5: Prediction of the convective time instant at which the flow is almost recovered to quasi-steady conditions

As mentioned in the previous chapter, the area under the increment of lift curve provides an idea of how much energy is put in the system during the gust encounter. The integral is computed from $\tilde{t} = 0$ to $\tilde{t} = 8.2$. According to figure 5.5, the gust effects at $\tilde{t} = 8.2$ are almost faded. Figure 5.6 shows again that the convolution of potential lift data with Wagner's function behaves very well. How-

ever, for high gust ratios the potential and quasi-steady model is more adequate for providing a closer value to real one.

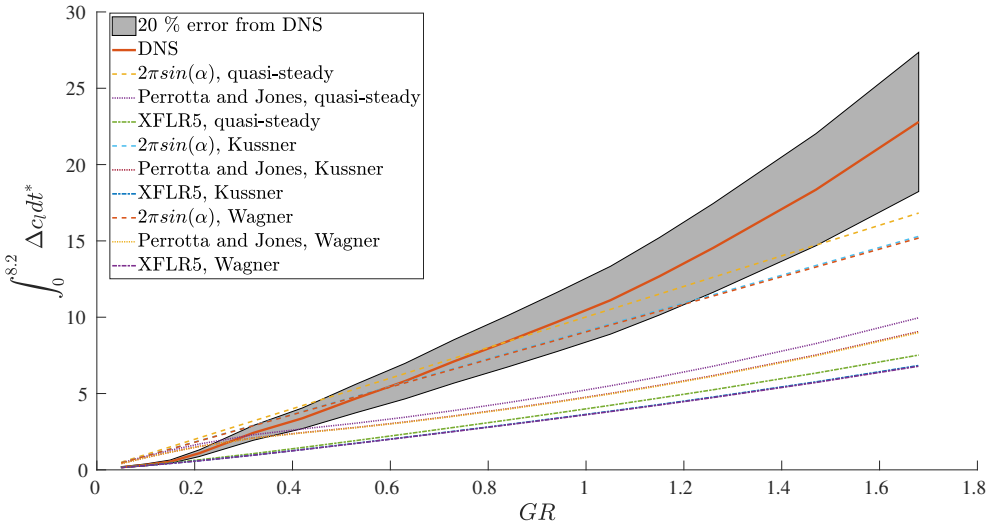

Figure 5.6: Integral of the increment of lift over time of different models

To end the discussion of this chapter, it has been seen that the thin airfoil theory is the best input data for the presented models. The next step is to choose between a quasi-steady or an unsteady model. The unsteady model would be a better option since it captures lift values after the gust as well. Moreover, Wagner's function seems to be a better choice for the convolution integrals instead of using Kussner's function: this is true because the analysis was made with respect to the heaving cases, where instantaneous changes of the effective angle of attack occur and α_{eff} is constant along the chordline (this is a necessary condition for using Wagner's function).

Chapter 6

Regulatory framework and socio-economic impact

6.1 Regulatory framework

To date, there are no regulations which determine requirements for MAVs related to gust envelopes. However, there are works such as which try to translate regulations for conventional aircrafts to micro air vehicles. The absence of specific requirements such as [17] limit load factors during a gust or any other limiting parameter related to gust envelopes is because of the current phase of development of these very small unmanned vehicles. The interest in these devices has arisen very recently, so that the certification authorities do not know to date the loads generated on a mini flapping wing device and there cannot be any regulations due to the current state of the art. In addition, this thesis is a computational analysis with the objective to acquire a better understanding of gust encounter at low Reynolds number flight regimes. Although there is a current discussion on the legal operating places for MAVs, those regulations would not affect to the aspects involved in this work. However, it is very likely to face specific regulation relating gust encounters for MAVs during the next 5-10 years.

Concerning risk analysis of the proposed solution for modelling gust encounters, the security of MAVs is not put in danger. For instance, the implementation of the unsteady model presented in Chapter 4 with the convolution of Wagner's function with thin airfoil theory lift data in flight control system may be a good starting point for the enhancement of the flight dynamic and control of MAVs.

6.2 Budget

A first component for the costs is the personnel expenses, which include the engineering hours without taking into account the cluster's usage. For this thesis, a total of 400 hours (approximately) where employed. A junior engineer in Spain may get paid 10€ per hour, so the personnel expenses rise to 4000€.

A second component for the total costs is the value of the resources used for the development of this work: a laptop, a DNS solver, a cluster and a MATLAB license. The laptop is currently worth 800€. Concerning the cluster, several CPUs where used for 1200 hours, amounting 240€ taking into account a cost of 0.2€/hour. The DNS solver may cost 9.000€, as an annual ANSYS FLUENT license. An annual MATLAB license is worth 800€.

Summing up all the costs for this project, the budget rises to a total cost of 14.840€.

6.3 Socio-economic impact of the project

To date, MAVs are designed without knowing their aerodynamic behavior due to winds' unsteadiness and many of them crash during a strong gust encounter and they remain destroyed, meaning a loss of resources for the users and an increment of costs for the user if he desires to buy another prototype.

The results presented in chapter 4 are very useful. The unsteady or quasi-steady model developed in this work can be implemented in the software governing the flight attitude and control of an MAV. The design of a better flight control system covering a larger envelope of gust encounters and load factors implies a lot of savings for current users of MAVs. The awareness if the loads generated during gust encounters will help structural analysts to design and manufacture wing without failing.

Therefore, the community interested in the use of MAVs will put trust into designers and manufacturers of these devices, meaning a considerable increase of demand as a consequence of a better offer. Then, the earnings for MAVs designers and manufactures shall grow a lot.

Concerning the ethical impacts, a large amount of high performance MAVs flying in our surroundings can violate the privacy right since these devices are able to execute master-spying missions. Regarding the environment, the increment of the use of MAVs may not be an environmental concern.

Thus, the enhancement of MAVs aerodynamic performance has a positive impact economically for both users and manufacturers, but it may not have such an excellent impact from the point of view of the ethics and people's privacy.

Chapter 7

Summary and conclusions

The purpose of this thesis is to get more insight about the unsteady phenomena of low Re flows around an airfoil during a strong transverse gust encounter. For that, there are analyzed the forces during discrete gust encounters at Re=1000 in order to be more familiar with the physics of the problem. It was performed a 2D DNS for different '1-cosine' gust profiles for a NACA0012 airfoil using TUCAN solver. The gusts were set to have the same gust width, so we only varied the gust ratio, which is a measure of gust intensity with respect to the free stream velocity.

At first, the gust was modelled as a plunge maneuver. After reuniting all the DNS results from the first computational setup, a parametric study was done in terms of gust ratio. It was seen that first peak lift during the gust increases linearly its magnitude with the gust ratio. The main responsible for this is the first LEV, whose intensity increases with GR. It was also seen that for high gust ratios, there is a significant second peak lift after the airfoil exits the gust. Concerning the drag, it increases and decreases during the gust with respect to the initial value, having a peak value near the gust end. The airfoil experiences some thrusting force during the gust encounter since the values of c_d decrease at some point with respect to the initial value of the drag. It was also seen that once the airfoil exits the gust, it takes several chord lengths, of the order of 10, for the flow to restabilize to the initial conditions prior the gust. Hence, the aerodynamic forces are affected both during and after the gust encounter.

In spite of the complexity of the problem (develop a suitable way for gust modelling and implement it within TUCAN), we wanted to explore different computational setups so that we could better mimic the gust encounters within the DNS solver. For that, a second setup was developed, were a travelling airfoil goes through a stationary vertical jet whose velocity profile is dictated by the gust ve-

locity profile. On top of the analysis of the previous set of results, it was noticed the role of a TEV when the airfoil's LE exits the gust, which influences the lift decay near the gust end due to the influence of the TEV on the suction surface. Moreover, the jet gusts suggested that the first lift peak may be lower in magnitude than the one yielded by the plunge maneuvers. This second setup may work very well for a 2D DNS, although it is more expensive than the first one, but it is not viable the use of this setup for a 3D simulation, were a huge amount of grid points would be needed. Therefore, the researcher may try to find other approaches for modelling gusts with a DNS solver. For that, it was proposed a third different computational setup in Chapter 4. This third setup may have, in principle, a lot of advantages: it is more realistic, it implies less computational costs and a 3D implementation is more affordable.

In view of the DNS results, high gust ratios may be a better design point since the loads are considerably larger compared to medium GR cases and the flight control system shall modify the flapping motion in order to overcome the changes in longitudinal and transversal forces.

After inspecting the DNS results, the next step was to elaborate some predicting models mainly for the lift force during and after the gust. Two different models are proposed: a quasi-steady one and an unsteady one. Both models need some input lift data and the gust profile. For the lift data, it was used data from Perrotta and Jones experiments [20], data from XFLR5 and data provided by the thin airfoil theory. It was observed that the best candidate for lift data inputs is the thin airfoil theory, which was very unexpected due to its strong assumptions incompatible with the characteristics of the flow regime during strong transverse gust encounters at low Re. It was seen that for high gust ratio cases, the quasi-steady models provide a better prediction than the indicial one. The indicial (unsteady) model with Wagner's function convolution provides better results for low or medium gust ratio cases, especially for the plunge maneuvers. It makes sense that the unsteady models work better at lower gust ratios since they are used in the aircraft industry for small displacements, assuming that no flow separation occurs. The main drawback of the quasi-steady model is that it does not capture recovery effects, as the unsteady model does thanks to the convolution approach with classical unsteady thin airfoil theory functions. Regarding the drag, the quasi-steady models were unable to predict properly the drag history. Note that even though the models show a satisfactory response for many cases, they do not take into account large displacements and flow separation, which are common features of the current problem.

After comparing results from both DNS setups and experiments from [20], it was observed an overestimation of lift values during plunge maneuvers with respect

to the experiments and the jet gust DNS, although the plunge maneuvers yield a good qualitative picture. Similarly to [20], we have discovered that the strength of the first emerging LEV is responsible of the peak lift during the gust. However, our database suggests that the recovery process takes a shorter time compared to the experiments. Hence, the results from the jet gust DNS and data from experiments, although they are performed at different conditions, indicate that the results from the plunge maneuvers may not be very representative for this current problem. It is not that the DNS results are not reliable or accurate, it is simply a modelling issue, that is why future works shall put an emphasis to simulate the gusts more realistically.

Regarding future works, the setup proposed in section 4.3 must be investigated and developed as a new approach for gust modelling in TUCAN. In addition, 3D simulations must be carried on for several reasons: identify if at Re=1000 there are 3D instabilities or effects which modify the time histories of lift and drag compared to 2D results. Moreover, it would be very desirable to compare future 3D results with 2D results and also DNS results with experiments done at the same conditions (Reynolds number, gust profile ...). This last exercise would help us discuss the DNS results based on the results and time histories given by equivalent experiments.

Regarding the predictive models, we must dive into other approaches which shall perform more satisfactorily or which may be able to cover a larger gust envelope, and they also should be able to predict the drag force during gust encounters. In addition, other models should take into account flow separation and dynamic stall phenomena. If lift data is needed for any other model, it should be found a more suitable source of data rather than the thin airfoil theory.

Chapter 8

Acknowledgements

First of all, I would like to express my most sincere gratitude to Prof. Manuel Moriche for making this project possible. Thank you for all your huge help, for your advices, for your patience and for all your efforts to open my mind (I know I am sometimes hard to deal with). Of course, I want to thank Óscar Flores for providing me the opportunity to work with the Computational Aerodynamics research group and for helping me alongside Manu during the thesis.

I would like to thank all my amazing colleagues I spent my time with during these last years. In particular, I want give my appreciation to Dani Sánchez, Adri and Dani Rubio. Thank you for your support and for all the joy we had during good and tough times.

I cannot forget about Ana and Raúl: you deserve more than a big "thank you" for our bond and for all the experiences, the good and the bad. My pride and happiness for knowing you and my most sincere respect for you cannot be expressed on this page.

Last but not least, I would like to take this opportunity to express from the bottom of my heart my respect and deepest gratitude to my parents for their unconditional love and support. I would not be what I am today without them.

Bibliography

[1] Introduction to aircraft aeroelasticity and loads, 2nd edition. *ProtoView*, 2(13), March 2015.

[2] Edward Albano and William P Rodden. A doublet-lattice method for calculating lift distributions on oscillating surfaces in subsonic flows. *AIAA journal*, 7(2):279–285, 1969.

[3] John David Anderson. *Fundamentals of aerodynamics*. McGraw-Hill. aeronautical and aerospace engineering. McGraw-Hill, New York [etc.], 5th ed. in si units. edition, 2011.

[4] Hulya Biler, Camli Badrya, and Anya R Jones. Experimental and computational investigation of transverse gust encounters. In *2018 AIAA Aerospace Sciences Meeting*, page 0571, 2018.

[5] James M. Birch and Michael H. Dickinson. Spanwise flow and the attachment of the leading-edge vortex on insect wings. *Nature*, 412(6848), August 2001.

[6] James M Birch, William B Dickson, and Michael H Dickinson. Force production and flow structure of the leading edge vortex on flapping wings at high and low reynolds numbers. *Journal of Experimental Biology*, 207(7):1063–1072, 2004.

[7] David L Brown, Ricardo Cortez, and Michael L Minion. Accurate projection methods for the incompressible navier–stokes equations. *Journal of computational physics*, 168(2):464–499, 2001.

[8] Diana D Chin and David Lentink. Flapping wing aerodynamics: from insects to vertebrates. *Journal of Experimental Biology*, 219(7):920–932, 2016.

[9] D Drikakis, D Kwak, and Cc Kiris. Computational aerodynamics: Advances and challenges. *Aeronautical Journal*, 120(1223):13–36, January 2016.

[10] Charles P. Ellington, Coen Van Den Berg, Alexander P. Willmott, and Adrian L. R. Thomas. Leading-edge vortices in insect flight. *Nature*, 384(6610), December 1996.

[11] Adam Hart, Michael Sytsma, and Lawrence Ukeiley. An aerodynamic characterization facility for micro air vehicle research. *International Journal of Micro Air Vehicles*, 8(2):79–91, 2016.

[12] Y. HOARAU, M. BRAZA, Y. VENTIKOS, D. FAGHANI, and G. TZABIRAS. Organized modes and the three-dimensional transition to turbulence in the incompressible flow around a naca0012 wing. *Journal of Fluid Mechanics*, 496(496):63–72, December 2003.

[13] Frederic M Hoblit. *Gust loads on aircraft: concepts and applications*. AIAA, 1988.

[14] Th von Kármán. Airfoil theory for non-uniform motion. *Journal of the Aeronautical Sciences*, 5(10):379–390, 1938.

[15] Herbert G Küssner. Zusammenfassender bericht über den instationären auftrieb von flügeln. *Luftfahrtforschung*, 13(12):410–424, 1936.

[16] Hao Liu, Charles P Ellington, Keiji Kawachi, Coen Van Den Berg, and Alexander P Willmott. A computational fluid dynamic study of hawkmoth hovering. *Journal of experimental biology*, 201(4):461–477, 1998.

[17] Andrzej Majka. Flight loads of mini uav. In *Solid State Phenomena*, volume 198, pages 194–199. Trans Tech Publ, 2013.

[18] Manuel Moriche Guerrero. *A numerical study on the aerodynamic forces and the wake stability of flapping flight at low Reynolds number*. Universidad Carlos III de Madrid, Departamento de Bioingenieria e Ingenieria Aeroespacial, Leganes, 2017.

[19] Thomas J Mueller. On the birth of micro air vehicles. *International Journal of Micro Air Vehicles*, 1(1):1–12, March 2009.

[20] Gino Perrotta and Anya Jones. Unsteady forcing on a flat-plate wing in large transverse gusts. *Experiments in Fluids*, 58(8):1–11, August 2017.

[21] Jitendra R Raol. *Mobile intelligent autonomous systems*. Taylor & Francis, Boca Raton, FL, 2012.

[22] W Shyy. *An introduction to flapping wing aerodynamics*. Cambridge aerospace series. Cambridge University Press, Cambridge [etc.], 2013.

[23] W. Shyy, H. Aono, S.K. Chimakurthi, P. Trizila, C.-K. Kang, C.E.S. Cesnik, and H. Liu. Recent progress in flapping wing aerodynamics and aeroelasticity. *Progress in Aerospace Sciences*, 46(7):284–327, 2010.

[24] W Shyy, Ck Kang, P Chirarattananon, S Ravi, and H Liu. Aerodynamics, sensing and control of insect-scale flapping-wing flight. *Proceedings Of The Royal Society A-Mathematical Physical And Engineering Sc*, 472(2186), February 2016.

[25] W. Shyy, Y. Lian, J. Tang, H. Liu, P. Trizila, B. Stanford, L. Bernal, C. Cesnik, P. Friedmann, and P. Ifju. Computational aerodynamics of low reynolds number plunging, pitching and flexible wings for mav applications. *Acta Mechanica Sinica*, 24(4):351–373, August 2008.

[26] Zachary F Smith, Anya R Jones, and John T Hrynuk. Micro air vehicle scale gust-wing interaction in a wind tunnel. In *2018 AIAA Aerospace Sciences Meeting*, page 0573, 2018.

[27] R. B. Srygley and A. L. R. Thomas. Unconventional lift-generating mechanisms in free-flying butterflies. *Nature*, 420(6916), December 2002.

[28] Markus Uhlmann. An immersed boundary method with direct forcing for the simulation of particulate flows. *Journal of Computational Physics*, 209(2):448–476, 2005.

[29] Coen van den Berg and Charles P. Ellington. The three-dimensional leading-edge vortex of a "hovering" model hawkmoth. *Philosophical Transactions: Biological Sciences*, 352(1351):329–340, 1997.

[30] Z Jane Wang. Two dimensional mechanism for insect hovering. *Physical review letters*, 85(10):2216, 2000.

[31] Z Jane Wang. Dissecting insect flight. *Annu. Rev. Fluid Mech.*, 37:183–210, 2005.

[32] C H K Williamson. Vortex dynamics in the cylinder wake. *Annual Review of Fluid Mechanics*, 28(1):477–539, 1996.

[33] Ralf Wokoeck, Rolf Radespiel, Hauke Ehlers, and Robert Konrath. Experimental and numerical investigations of pitch-plunging wing aerodynamics at low reynolds number. *International Journal of Engineering Systems Modelling and Simulation 47*, 5(1-3):19–32, 2013.